



Michigan Technological University  
*Create the Future* Digital Commons @ Michigan Tech

---

Dissertations, Master's Theses and Master's  
Reports - Open

Dissertations, Master's Theses and Master's  
Reports

---

2010

## Investigation into the impact of grain boundaries, film interface, and crystallographic orientation on the ionic conductivity of thin film gadolinium-doped ceria

Matthew M. Swanson  
*Michigan Technological University*

Follow this and additional works at: <https://digitalcommons.mtu.edu/etds>

 Part of the [Engineering Science and Materials Commons](#)


Copyright 2010 Matthew M. Swanson

---

### Recommended Citation

Swanson, Matthew M., "Investigation into the impact of grain boundaries, film interface, and crystallographic orientation on the ionic conductivity of thin film gadolinium-doped ceria", Dissertation, Michigan Technological University, 2010.  
<https://doi.org/10.37099/mtu.dc.etds/19>

Follow this and additional works at: <https://digitalcommons.mtu.edu/etds>

 Part of the [Engineering Science and Materials Commons](#)

INVESTIGATION INTO THE IMPACT OF GRAIN BOUNDARIES, FILM INTERFACE,  
AND CRYSTALLOGRAPHIC ORIENTATION ON THE IONIC CONDUCTIVITY OF  
THIN FILM GADOLINIUM-DOPED CERIA

By

MATTHEW M. SWANSON

A DISSERTATION

Submitted in partial fulfillment of the requirements

for the degree of

DOCTOR OF PHILOSOPHY

(Materials Science and Engineering)

MICHIGAN TECHNOLOGICAL UNIVERSITY

2010

© 2010 Matthew M. Swanson

This dissertation, "INVESTIGATION INTO THE IMPACT OF GRAIN BOUNDARIES, FILM INTERFACE, AND CRYSTALLOGRAPHIC ORIENTATION ON THE IONIC CONDUCTIVITY OF THIN FILM GADOLINIUM-DOPED CERIA", is hereby approved in partial fulfillment of the requirements for the degree of DOCTOR OF PHILOSOPHY in the field of Materials Science and Engineering.

DEPARTMENT:  
Materials Science and Engineering

Signatures:

Dissertation Advisor \_\_\_\_\_  
Dr. Peter D. Moran

Department Chair \_\_\_\_\_  
Dr. Mark R. Plichta

Date \_\_\_\_\_

For my dearest wife and two beautiful children.

# Contents

|  |          |
|--|----------|
| List of Figures  | ix       |
| List of Tables   | x        |
| Preface  | xi       |
| Acknowledgments  | xiii     |
| Abstract   | xv       |
| <b>1 Introduction</b>  | <b>1</b> |
| <b>2 Impact of the presence of grain boundaries on the in-plane ionic conductivity of thin film Gd-doped CeO<sub>2</sub></b> | <b>8</b> |
| 2.1 Abstract . . . . .   | 9        |
| 2.2 Introduction . . . . .   | 10       |
| 2.3 Experimental Methods . . . . .   | 11       |
| 2.4 Results and Discussion . . . . .   | 13       |

|          |   |           |
|----------|---|-----------|
| 2.5      | Conclusions . . . . .   | 25        |
| <b>3</b> | <b>Impact of the surface/interface on the ionic conductivity of thin film Gd-doped CeO<sub>2</sub></b>  | <b>27</b> |
| 3.1      | Abstract . . . . .  | 28        |
| 3.2      | Introduction . . . . .  | 28        |
| 3.3      | Experimental Methods . . . . .  | 31        |
| 3.4      | Results and Discussion . . . . .  | 32        |
| 3.5      | Conclusions . . . . .   | 42        |
| <b>4</b> | <b>Impact of the crystallographic orientation on the ionic conductivity of thin film Gd-doped CeO<sub>2</sub></b>                                   | <b>44</b> |
| 4.1      | Abstract . . . . .  | 45        |
| 4.2      | Introduction . . . . .  | 45        |
| 4.3      | Experimental Methods . . . . .  | 46        |
| 4.4      | Results and Discussion . . . . .  | 47        |
| 4.5      | Conclusions . . . . .   | 54        |
| <b>5</b> | <b>Discussion: Cause of the reduced conductivity observed in samples with grain boundaries and the reduced conductivity surface/interface layer</b> | <b>56</b> |
| 5.1      | Introduction . . . . .  | 57        |
| 5.2      | Explanation of the reduced conductivity observed in the polycrystalline GDC compared to the single crystal GDC . . . . .                            | 57        |

|          |   |           |
|----------|---|-----------|
| 5.3      | Explanation of the reduced conductivity in the interface layer of GDC films . . . . . | 59        |
| 5.4      | Conclusions . . . . .   | 63        |
| <b>6</b> | <b>Summary</b>  | <b>64</b> |
|          | <b>Bibliography</b>   | <b>67</b> |
|          | <b>Appendix A</b>   | <b>70</b> |
|          | <b>Appendix B</b>   | <b>75</b> |

# List of Figures

|     |  |    |
|-----|--|----|
| 1.1 | Typical fuel cell polarization plot. . . . .   | 3  |
| 1.2 | Cubic Fluorite structure of GDC. . . . .   | 5  |
| 2.1 | The surface morphology of the $\approx 300$ nm (001)-oriented single-crystal GDC film grown on the single crystal $\text{CeO}_2$ -buffered r-plane sapphire substrate. a) $5 \times 5 \mu\text{m}$ 3D height image with y axis increment = 12 nm/div. b) $5 \times 5 \mu\text{m}$ phase contrast image c) $1 \times 1 \mu\text{m}$ 3D height image data with y axis increment = 12 nm/div d) $1 \times 1 \mu\text{m}$ phase-contrast image. No grain boundaries are apparent in the single-crystal film. . .   | 17 |
| 2.2 | The surface morphology of the $\approx 300$ nm thick highly oriented (111) polycrystalline GDC films grown on as received r-plane sapphire substrate. a) $5 \times 5 \mu\text{m}$ 3D height image with y axis increment = 12 nm/div. b) $5 \times 5 \mu\text{m}$ phase contrast image c) $1 \times 1 \mu\text{m}$ 3D height image data with y axis increment = 12 nm/div d) $1 \times 1 \mu\text{m}$ phase-contrast image. The polycrystalline film consists of sub-micron grains. . . . .   | 18 |
| 2.3 | Comparison of $\theta/2\theta$ XRD data from the $\approx 300$ nm GDC film grown on the as-received $\text{Al}_2\text{O}_3$ substrate (denoted as "(111) GDC"), with the data for the $\approx 300$ nm GDC film grown on the un-doped 38 nm $\text{CeO}_2$ -buffered substrate (denoted as "(001) GDC") and the data recorded from a the 35 nm single-crystal (001) $\text{CeO}_2$ buffer layer with no subsequent GDC growth (denoted as "(001) CEO"). The GDC grown on the as-received sapphire is of mixed orientation, with most of the film consisting of (111)-oriented material where the GDC grown on the buffered substrate consists entirely of material with a (001) orientation. . . . . | 19 |



|     |   |    |
|-----|---|----|
| 2.4 | XRD $\phi$ - scan data for the $\approx 300$ nm (001) GDC grown on the buffered sapphire substrate. The 4-fold symmetry of the asymmetric (204) GDC peaks shows the in-plane epitaxial relationship between the GDC film and the sapphire substrate and demonstrates that the (001) GDC film is single-crystal. . . . .   | 20 |
| 2.5 | a) Rocking curve of (111) peak of highly oriented polycrystalline GDC with $\approx 300$ nm thickness and b) Rocking curve of (002) plane of the epitaxial GDC film. Scans were done with count time = 2, step size = $0.05^\circ$ for (111) GDC. The lower step size = $0.015^\circ$ is used for (002) GDC at the same count rate. . . . .   | 21 |
| 2.6 | The plot of $\ln(\sigma T)$ as a function of $1000/T$ of (111) GDC polycrystalline film with boundaries separating submicron grains and (001) epitaxial film with no grain boundaries. The presence of the grain boundaries significantly reduces the ionic conductivity of GDC over the entire temperature range. . . . .  | 22 |
| 2.7 | The total conductivity of submicron grained GDC samples as a function of a reciprocal of temperature ( $T$ ) $\times 1000$ for the highest published data sets collected in the 400-700°C range. Values given under the researchers name provide the reported grain size for each data set. Epitaxial, single crystal GDC data provided by Chen et al. [1] aligns almost identically with the single crystal data from this study, but were not included in the plot for clarity. . . . . | 23 |
| 3.1 | Symmetric $\theta/2\theta$ X-ray diffraction data from the 500 nm GDC film showing the [001] out-of-plane orientation. The center peak is from the sapphire substrate. . . . .  | 33 |
| 3.2 | XRD $\phi$ -scan data for the 500 nm (001) GDC film. The 4-fold symmetry of the asymmetric (204) GDC peaks shows that a single in-plane epitaxial relationship exists between the GDC film and the sapphire substrate demonstrating that the film is a single-crystal. . . . .  | 34 |
| 3.3 | Arrhenius plot showing conductivity of five films of varying thickness. Uncertainties are less than the symbol size unless otherwise shown. The conductivities of the two thinnest films are dramatically reduced compared to those of the thicker films. . . . .   | 35 |

|     |   |    |
|-----|---|----|
| 3.4 | Schematic conductance versus thickness plot showing possible impacts of a film surface/interface. Figure inset shows bulk, $C_B$ , and interface, $C_I$ conductance paths in the two layer model. . . . . | 37 |
| 3.5 | Conductance data for 5 single crystal GDC films at 500°C. . . . .   | 39 |
| 3.6 | Conductance data for 5 single crystal GDC films at 700°C. . . . .   | 40 |
| 3.7 | Arrhenius plot showing the bulk and interface components of the five GDC films. The data from the bulk component of the 500 nm film lies directly under the bulk component of the 110 nm film. . . . .    | 43 |
| 4.1 | Schematic showing the relative positions of the atomic sites on two adjacent (100) planes. The flux plane is denoted as a dashed line. . .  | 51 |
| 4.2 | Schematic showing the relative positions of the atomic sites on four adjacent (110) planes. The flux plane is denoted as a dashed line. . .   | 52 |
| 5.1 | Plot of the $\theta/2\theta$ data for the (002) reflection of the five GDC films and the CEO buffer layer. . . . .  | 61 |
| 5.2 | Plot of the $\theta/2\theta$ data for the (004) reflection of the five GDC films and the CEO buffer layer. . . . .  | 62 |
| 6.1 | Schematic showing the relative positions of the atomic sites on two adjacent (100) planes. The flux plane is denoted as a dashed line. . .  | 76 |
| 6.2 | Schematic showing the relative positions of the atomic sites on four adjacent (110) planes. The flux plane is denoted as a dashed line. . .   | 77 |

# List of Tables

|     |  |    |
|-----|--|----|
| 2.1 | Single crystal (001)-oriented GDC without grain boundaries: Summary of data used to calculate the temperature dependent conductivity. . .  | 20 |
| 2.2 | Polycrystalline (111)-oriented GDC with sub-micron grains: Summary of data used to calculate the temperature dependent conductivity. . .   | 21 |
| 2.3 | Polycrystalline (111)-oriented GDC with sub-micron grains: Summary of data used to calculate the temperature dependent conductivity. . .   | 22 |
| 2.4 | A comparison of GDC $\ln(\sigma T)$ vs $(1/T)$ data for thin film GDC in the literature. Activation energy ( $E_a$ ), conductivity ( $\sigma$ ), and the Y-intercept ( $\ln(\sigma T)$ ), were extracted by analyzing published plots of literature data. . . . .  | 23 |
| 3.1 | Conductivity data for single crystal GDC films with varying thickness. The uncertainties represent 1 standard deviation in the fit of the data.  | 36 |
| 3.2 | Extracted $\ln(\sigma T)$ -intercepts and activation energies characterizing the bulk and interface conduction paths. This data represents the average conductivity values calculated for the bulk and interface paths from the 110, 278, and 500 nm samples. The uncertainties represent 1 standard deviation in the fit of the data. . . . . | 41 |
| 4.1 | Comparison of the average conductivity data for the [100] and [110] orientations in the 540 to 700°C temperature range. The uncertainties represent 1 standard deviation in the fit of the data. . . . .   | 53 |

# Preface

This preface serves as an explanation of the author's role in the work that comprises each of the chapters that make up the body of this dissertation. The body of this dissertation is made up of three bodies of work : (1) Impact of the presence of grain boundaries on the in-plane ionic conductivity of thin film Gd-doped  $\text{CeO}_2$ , (2) Impact of the surface/interface on the ionic conductivity of thin film Gd-doped  $\text{CeO}_2$ , and (3) Impact of the crystallographic orientation on the ionic conductivity of thin film Gd-doped  $\text{CeO}_2$ . The first body of work has been published in Solid State Ionics and the permission to reprint it is given in a document in the Appendix. The second body of work has been submitted to Solid State Ionics, underwent revisions and is awaiting a final decision. The third body of work has not yet been submitted to a journal.

My contributions to the work reported in Chapter 2 include development of the high temperature conductivity measurement stand, dicing of films and sample preparation, collection of all of the conductivity data, analysis of conductivity data and sole writing of the paper.

My contributions to the work reported in Chapter 3 include growth of the new single crystal films, XRD and AFM structural characterization of the films, dicing of films and sample preparation, collection of all of the conductivity data, analysis of conductivity data and sole writing of the paper.

My contributions to the work reported in Chapter 4 include growth of a new single crystal film, XRD structural characterization of the film, dicing of film and sample preparation, collection of all of the conductivity data, analysis of conductivity data and sole writing of the paper.

# Acknowledgments

I would like to thank Dr. Peter Moran for all of his help and guidance during my Ph.D. program. There have been countless times when I have been just "spinning my wheels" while trying to solve a problem and he has been able to redirect my progress to a productive path. He has taught me to be satisfied with adding to the body of knowledge on a subject instead of feeling like we need to fully explain every aspect of the system. Lastly, he has been a good friend with whom I have shared in many interesting and encouraging conversations.

I would like to thank my fellow research group members and friends, Madhana Sunder, Natee Tangtrakarn, Lakshmi Krishna, and Aaron Lalonde. They have been a great source of knowledge and support as we worked through our collective research problems together. We might have been able to graduate without each other, but it sure wouldn't have been as much fun!

I would like to thank Department of Defense for SMART scholar fellowship that funded a large part of my Ph.D. studies. This support allowed me to work comfortably and without the constant stress of discontinued funding.

Lastly, I would like to thank my wife for the years of support and understanding. Thank you for having just as much commitment to my goal as I did. This has truly

been a team effort.

# Abstract

The research reported in this dissertation investigates the impact of grain boundaries, film interface, and crystallographic orientation on the ionic conductivity of thin film Gd-doped  $\text{CeO}_2$  (GDC).

Chapter 2 of this work addresses claims in the literature that submicron grain boundaries have the potential to dramatically increase the ionic conductivity of GDC films. Unambiguous testing of this claim requires directly comparing the ionic conductivity of single-crystal GDC films to films that are identical except for the presence of submicron grain boundaries. In this work techniques have been developed to grow GDC films by RF magnetron sputtering from a GDC target on single crystal r-plane sapphire substrates. These techniques allow the growth of films that are single crystals or polycrystalline with 80 nm diameter grains. The ionic conductivities of these films have been measured and the data shows that the ionic conductivity of single crystal GDC is greater than that of the polycrystalline films by more than a factor of 4 over the 400-700°C temperature range.

Chapter 3 of this work investigates the ionic conductivity of surface and interface regions of thin film Gd-doped  $\text{CeO}_2$ . In this study, single crystal GDC films have been grown to thicknesses varying from 20 to 500 nm and their conductivities have been measured in the 500-700°C temperature range. Decreasing conductivity with



decreasing film thickness was observed. Analysis of the conductivity data is consistent with the presence of an approximately 50 nm layer of less conductive material in every film. This study concludes that the surface and interface regions of thin film GDC are less conductive than the bulk single crystal regions, rather than being highly conductive paths.

Chapter 4 of this work investigates the ionic conductivity of thin film Gd-doped  $\text{CeO}_2$  (GDC) as a function of crystallographic orientation. A theoretical expression has been developed for the ionic conductivity of the [100] and [110] directions in single crystal GDC. This relationship is compared to experimental data collected from a single crystal GDC film. The film was grown to a thickness of  $\approx 300$  nm and its conductivity measured along the [100] and [110] orientations in the 500-700°C temperature range. The experimental data shows no statistically significant difference in the conductivities of the [100] and [110] directions in single crystal GDC. This result agrees with the theoretical model which predicts no difference between the conductivities of the two directions.

# Chapter 1

## Introduction

Growing energy demand and volatility in fuel prices has motivated interest in developing efficient, fuel flexible energy converters. Fuel cells have the potential to fill this role due to their high efficiencies in directly converting chemical energy to electricity. Solid oxide fuel cells are a type of fuel cell that is well suited to handling a wide variety of fuels and exhibit high conversion efficiencies. It is necessary to further improve the cost, efficiency and lifetime of SOFCs. The cost and life time of SOFCs can be improved by reducing their operating temperature from high temperatures (800-1100°C) to intermediate temperatures (500-700°C). This reduction in temperature reduces cost by allowing the use of less expensive metals, instead of ceramic components, for "balance of system" components and increases the lifetime by reducing harmful diffusion between the fuel cell components. However, the reduction

in temperature also reduces the "kT" available to assist the thermally activated processes occurring in the fuel cell components and thereby reduces the efficiency. Fuel cells are electrochemical devices that convert chemical energy to electricity. The three active components of a fuel cell are the anode, cathode and electrolyte. The anode and cathode act as catalysts to the reduction/oxidation reactions that occur at the interface between them and the electrolyte. The electrolyte conducts ions between the electrodes and acts as a barrier for gas and electron flow. The efficiency of a fuel cell is, in general, a function of the current density,  $J$ , defining the conditions of operation. The electrolyte resistance is one of four types of mechanisms that reduce the efficiency of fuel cells. Fuel cell efficiency can be expressed by dividing the observed voltage,  $V(J)$ , by the Nernst voltage,  $E_{Nernst}$ . The observed voltage produced across a fuel cell operating with a current density "J" is determined by the Nernst voltage minus four loss terms as shown in Equation 1.0.1.

$$V(J) = E_{Nernst} - \eta_{Parasitic} - \eta_{Activation} - \eta_{Ohmic} - \eta_{Concentration} \quad (1.0.1)$$

The  $\eta$  terms are related to different loss mechanisms.  $\eta_{Parasitic}$  losses arise from electron and gas leakage across the electrolyte.  $\eta_{Activation}$  losses are due to kinetic limitations of reactions occurring at the boundary between electrodes, fuel/oxidant, and the electrolyte (the "triple phase boundary").  $\eta_{Ohmic}$  losses result primarily from resistance to ionic motion in the electrolyte.  $\eta_{Concentration}$  describes losses are due to having insufficient amounts of the fuel/oxidant available at the triple phase boundary

due to mass transport limitations. The plot of observed voltage versus current density is the polarization curve. A typical fuel cell polarization curve identifying the regions in which each loss dominates is shown in Figure 1.1.

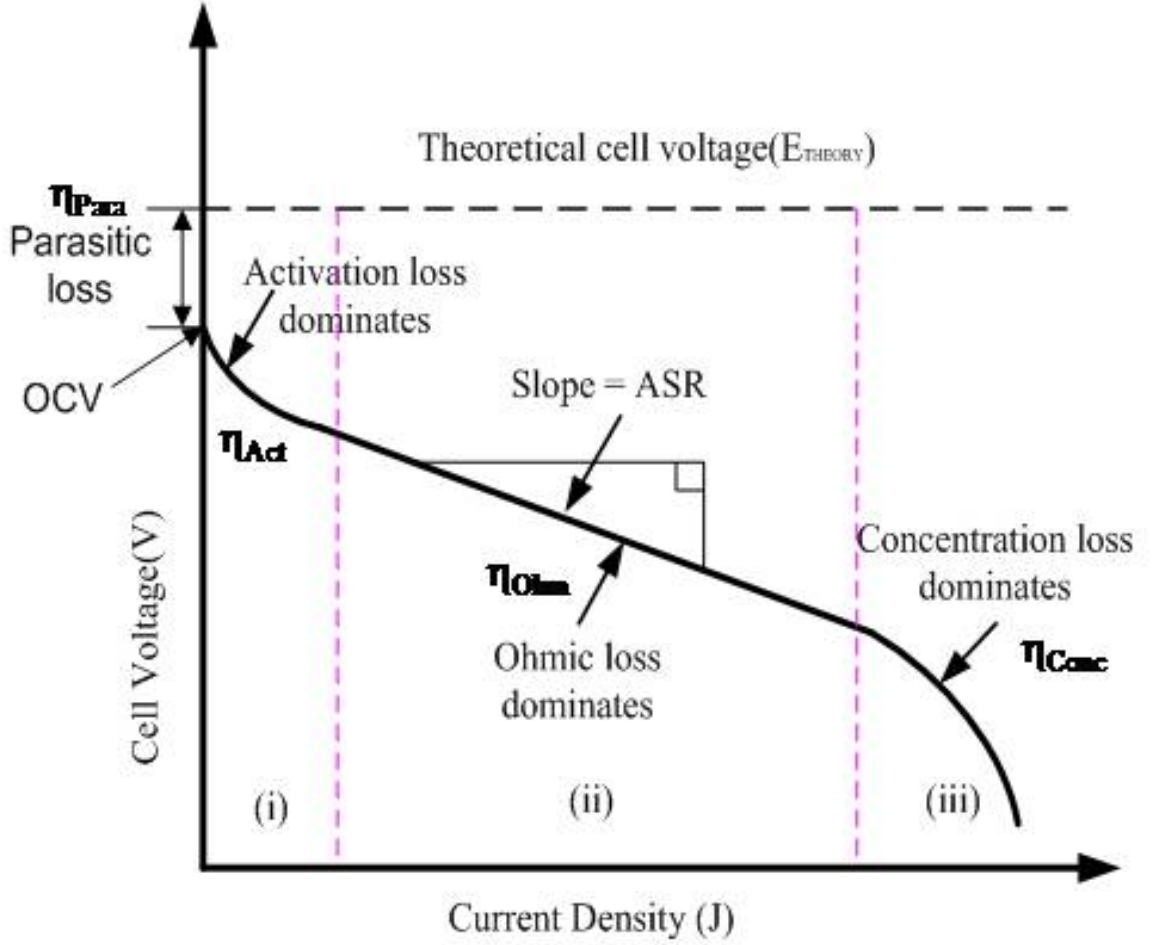


**Figure 1.1:** Typical fuel cell polarization plot.

This study focuses on the electrolyte and, consequently, the ohmic loss term,  $\eta_{Ohmic}$ .

The expression for the ohmic loss as a function of electrolyte resistance is:

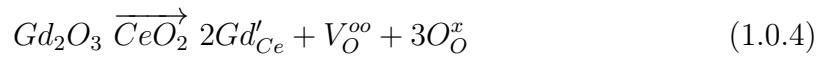
$$\eta_{Ohmic} = J \frac{L}{\sigma_i} = J * r_{area} \quad (1.0.2)$$

Where  $J$  (A/cm<sup>2</sup>) is the current density,  $L$  (cm) is the length of ionic travel in the electrolyte,  $\sigma_i$  (1/Ω-cm) is the ionic conductivity of the electrolyte, and  $r_{area}$  (Ω-cm<sup>2</sup>) is the area specific resistance of the electrolyte. Equation 1.0.2 indicates that  $\eta_{Ohmic}$  can be reduced by decreasing the length of ionic travel in the electrolyte or increasing the ionic conductivity. This study concentrates on determining the impact of grain boundaries and interfaces on the ionic conductivity of the material. The ionic conductivity of the electrolyte can be expressed as the product of the charge carrier concentration,  $[V_o^{oo}]$  (oxygen vacancies/cm<sup>3</sup>), the charge on each carrier, "q" (Coulombs), and the mobility of the charge carriers,  $\mu$  (cm<sup>2</sup>/V-sec) as shown in Equation 1.0.3.

$$\sigma_i(T) = V_o q \mu \quad (1.0.3)$$

Gadolinia doped Ceria (GDC) is a SOFC electrolyte material with comparatively high ionic conductivity at intermediate temperatures (500-700°C). It has the same cubic fluorite structure of undoped CeO<sub>2</sub> (CEO) shown in Figure 1.2.

An increase in the ionic conductivity of CeO<sub>2</sub> occurs upon doping with Gd due to an increased density of oxygen vacancies that occurs to maintain charge neutrality. One oxygen vacancy is created for every two Trivalent Gadolinium atoms that replace quad-valent cerium atoms in the crystal structure according to Equation 1.0.4.



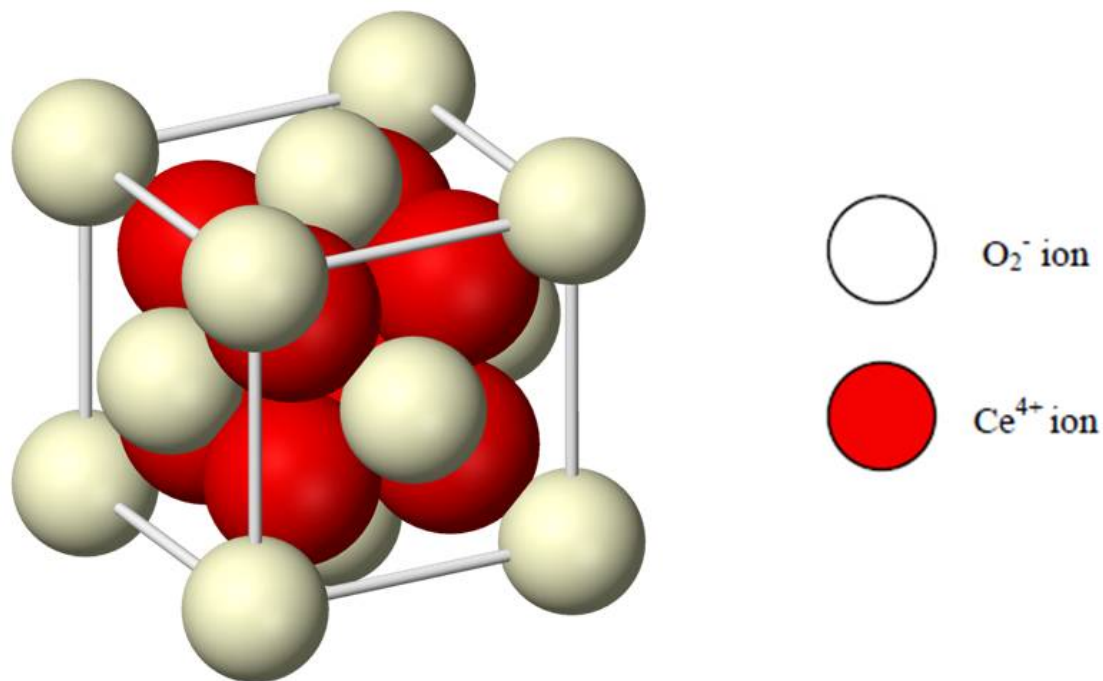


**Figure 1.2:** Cubic Fluorite structure of GDC.

This relationship can be used to estimate the number of oxygen vacancies, but vacancy clustering and environmental influences (oxygen partial pressure and temperature) prohibit accurate quantitative use.

The ionic conduction in the electrolyte occurs by the vacancy mechanism. Oxygen vacancies, created through the doping process, allow the movement of oxygen ions through the GDC structure. Oxygen ions hop from vacancy to vacancy in the direction of the decreasing chemical potential gradient. For fuel cells, this gradient is caused by the difference in oxygen concentrations at the two sides of the electrolyte. Ions must overcome a potential barrier, called the Gibbs Free Energy of migration ( $\Delta G_m$ ), to move into the neighboring vacant lattice site. The height of this barrier,

$\Delta G_m$ , is determined by the electric static repulsive forces on the ion due to the nearby cations between the ion and the vacancy position. Loss due to the electrolyte,  $\eta_{Ohmic}$ , is very small when "kT" is large compared to the barrier energy, but increases as the two values become comparable.

The commonly accept equation expressing the ionic conductivity in terms of the oxygen vacancy fraction,  $n_v$ , and height of the migration barrier,  $\Delta G_m$  ( $\Delta G_m = \Delta H_m - \Delta S_m T$ ), is shown in Equation 1.0.5.

$$\sigma_i(T) = (1 - N_v) C q \mu_i = \frac{N_v (1 - N_v) C z q^2 a_o^2 f \nu_o}{6 k T} \exp\left(\frac{\Delta S_m}{k}\right) \exp\left(\frac{-\Delta H_m}{k T}\right) \quad (1.0.5)$$

Where  $N_v$  is the fraction of equivalent oxygen sites that are vacant (unitless),  $C$  is the concentration of oxygen sites (sites per  $\text{cm}^3$ ),  $q$  is the charge on an ion ( $2 \times 1.602 \times 10^{-19} \text{C}$ ),  $\mu_i$  is the ion mobility ( $\text{cm}^2 \text{V}^{-1} \text{sec}^{-1}$ ),  $z$  is the coordination number for the oxygen sites (6),  $a_o$  is the lattice spacing ( $2.72 \times 10^{-8} \text{ cm}$  in GDC),  $f$  is a correlation factor (0.65 for cubic lattices),  $\nu_o$  is the vibrational frequency of the lattice (about  $10^{12}$ - $10^{13}$ ),  $k$  is Boltzmann's constant ( $8.617 \times 10^{-8} \text{ eV/K}$ ),  $T$  is temperature (K),  $\Delta S_m$  is the entropy of migration ( $\Delta S_m/k$  2.3), and  $\Delta H_m$  is the enthalpy of migration (eV). Inspection of Equation 1.0.5 shows that many of the terms can be expressed as constants that depend on the type of electrolyte material and do not change with  $N_v$  and  $\Delta H_m$ . The only variables for this GDC electrolyte system are  $N_v$  and  $\Delta H_m$ .

While experimental measurement of the vacancy concentration is difficult, measurement of the migration enthalpy is readily accomplished. Equation 1.0.5 can be recast into an Arrhenius equation that can be used to extract the enthalpy of migration,  $\Delta H_m$ , from  $\sigma$  vs.  $T$  measurements.

$$\ln(\sigma_i T) = -\frac{\Delta H_m}{k} \frac{1}{T} + \ln\left[\frac{N_v(1 - N_v)Czq^2a_o^2f\nu_o}{6k} \exp\left(\frac{\Delta S_m}{kT}\right)\right] \quad (1.0.6)$$

This equation shows that by plotting  $\ln(\sigma T)$  vs.  $1/T$  and finding the slope of the data, the enthalpy of migration can be obtained. This analysis is commonly used for the comparison of electrolytes.

Recently, the measurement and enhancement of the ionic conductivity of Gadolinium doped Ceria (GDC) has been an active area of research [2–9]. Numerous researchers have investigated the effect of grain boundaries on the ion conductivity of GDC [2–4, 10–16] and some have reported a significant enhancement of ionic conductivity in GDC with grain sizes  $< 200$  nm when compared to larger grained samples [3, 11–13, 16]. Chapter 2 of this work further investigates the role of grain boundaries on the ionic conductivity of GDC by the growth and electrical characterization of two GDC films that differ only by the presence or absence of grain boundaries.



## Chapter 2

# Impact of the presence of grain boundaries on the in-plane ionic conductivity of thin film Gd-doped CeO<sub>2</sub>

Authors: Matthew Swanson, Natee Tangtrakarn, Madhana Sunder, and P.D. Moran

## 2.1 Abstract

Though reports in the literature have been interpreted as indicating that the presence of boundaries between submicron grains has the potential to dramatically increase the ionic conductivity of Gd-doped  $\text{CeO}_2$  (GDC) films [2–4], unambiguous interpretation is hampered by the lack of a study directly comparing the ionic conductivity of single-crystal GDC films to films that are identical except for the presence of submicron grain boundaries. Techniques are developed to grow GDC films by RF magnetron sputtering from a (10%) $\text{Gd}_2\text{O}_3$ -(90%) $\text{CeO}_2$  target onto a single crystal r-plane sapphire substrate that, though otherwise are largely identical, differ in that one film is a single crystal while the other is polycrystalline with  $\approx 80$  nm diameter grains. The ionic conductivity of these films is measured in the temperature range of 400-700°C in the Van der Pauw geometry. Analysis of the  $\ln(\sigma T)$  vs.  $1/T$  data reveals the single crystal and polycrystalline GDC thin films differ primarily in that the single crystal film exhibits a lower activation energy for ionic conduction of  $0.85 \pm 0.01$  eV than the  $0.99 \pm 0.01$  eV observed for ionic conduction in the polycrystalline film. The presence of 80 nm grains reduces the ionic conductivity of Gd-doped  $\text{CeO}_2$  in the temperature range of 400-700°C.

Keywords: Single crystal, Van der Pauw, SOFC, GDC

## 2.2 Introduction

The ionic conductivity of submicron grained Gd-doped  $\text{CeO}_2$  (GDC) films is an area of active investigation [2–4, 8, 15, 17] motivated by the role of the material as an enabling electrolyte for enhanced intermediate temperature solid oxide fuel cells (IT-SOFCs). Reports in the published literature have shown a trend of increasing ionic conductivity with decreasing grain size for GDC in the submicron grain region [2–4]. This observation seems to have lead to the conclusion that submicron grains enhance the ionic conductivity of GDC, but the observed enhancement has only been shown in relation to coarser grained GDC and not to single crystal GDC. An experimental investigation that directly tests the effects of submicron grains by comparing the in-plane conductivity of GDC films that are largely identical except for the presence or absence of grain boundaries would address this question, but is absent from the literature.

In this work, the effect of submicron grain boundaries on the in-plane ionic conduction of GDC thin films is examined. The approach taken to isolate the effects of grain boundaries on conductivity is to grow single-crystal and polycrystalline GDC films on highly insulating r-plane  $\text{Al}_2\text{O}_3$  substrates that are otherwise identical and to make precise measurements of the ionic conductivity of the two types of films in the temperature range of 400-700°C using the Van der Pauw geometry. While it is straightforward to grow polycrystalline GDC films on highly insulating  $\text{Al}_2\text{O}_3$  sub-

strates by RF magnetron sputtering, methods for depositing single-crystal thin-film GDC on  $\text{Al}_2\text{O}_3$  substrates (no grain boundaries) have not been reported and so are developed here. Growth of epitaxial single crystal GDC films would typically require a modification of growth conditions from those employed to grow the polycrystalline film that could potentially change the Gd-content of the deposited film and so exhibit differences in ionic conductivity that are not due to the presence or absence of grain boundaries. The approach taken here to minimize the potential impact of these changes in growth conditions is to examine whether deposition of a  $\approx 30$  nm un-doped single crystal  $\text{CeO}_2$  buffer layer on the  $\text{Al}_2\text{O}_3$  prior to GDC film growth, under deposition conditions that would otherwise result in polycrystalline GDC with a sub-micron grain size, can engender the growth of single crystal GDC.

## 2.3 Experimental Methods

The GDC films that are the subject of this study were grown by RF magnetron sputtering from a (10%) $\text{Gd}_2\text{O}_3$ -(90%) $\text{CeO}_2$  target. Deposition parameters were held constant at the following values to ensure equal dopant concentrations in the films: A power density of 19.1 Watts/sq inch was applied to the target, a substrate-target distance of 9 cm was maintained, and an environment consisting of Ar/ $\text{O}_2$  in a ratio of 4:1 was kept at 5 mTorr during growth on a substrate held at a temperature of 830°C. One set of films was grown to  $\approx 300$  nm directly on a 2" diameter r-plane

sapphire substrate while the other set was grown to the same thickness on a 38 nm un-doped single crystal (001)  $\text{CeO}_2$  buffer layer that had been previously deposited on a 2" diameter r-plane  $\text{Al}_2\text{O}_3$  substrate. The methods developed to grow single crystal (001)  $\text{CeO}_2$  have been described in a previous publication [18].

Atomic force microscopy (AFM), X-ray diffraction (XRD), and spectrally resolved optical reflectance were used to structurally characterize the GDC films. The surface morphology of the films and the presence or absence of sub-micron grains in the GDC films were characterized using the phase contrast mode of atomic force microscopy. X-ray diffraction scans were used to determine the orientation of the thin films and whether the films were single crystal or polycrystalline. The precise thickness of each set of films was measured by spectrally resolved optical reflectance. The wafers were then diced into 1 cm x 1 cm squares for subsequent electrical characterization.

Conductivity data was recorded as a function of temperature for 7 data points between 400-700°C. The temperature dependence of the ionic conductivity was measured by attaching four Pt wires to the four corners of the samples with  $\approx 1$  mm triangles of platinum paint in the Van der Pauw geometry. The Van der Pauw method has the advantage over other four-point conductivity tests in that it more robustly results in precise conductivity measurements from thin films free from potential impact on the measurement of contact resistance, uniform probe spacing, or sample size [19]. Though no special measures were taken to block electronic conduction while mea-

suring ionic conductivity values, the electronic conductivity is taken to be negligible since the electrolytic domain boundary occurs at an oxygen partial pressure that is roughly 17 orders of magnitude lower than that used in this experiment [8]. Each measurement of the conductivity at a given temperature is the result of averaging 3 sets of eight measured voltages. The uncertainties reported for the conductivity measurements represent the standard deviation of 3 conductivity measurements obtained by 24 voltage measurements for each film at each temperature, so that the data reported here summarize the result of 336 individual voltage measurements. Since data reported here was recorded from one polycrystalline sample and one single crystal sample, the uncertainties reported do not capture any differences in the measurement results that could occur due to differences between samples or in electrode geometries. These differences are unlikely to be significant in that the film deposition process is quite reproducible and previous studies [20] have demonstrated that small variations in the type of electrode geometry employed in this study does not significantly perturb the measurement results.

## 2.4 Results and Discussion

Atomic force microscopy, X-ray diffraction, and spectrally resolved reflectance characterization reveal that the two sets of films differ in that the film grown on the  $\text{CeO}_2$  template is single crystal, whereas that grown directly on the sapphire substrate is

polycrystalline. The morphology of the GDC film grown on the 38 nm undoped (001) CeO<sub>2</sub> template is shown in the AFM data of Figure 2.1, whereas that of the film grown directly on the sapphire substrate is shown in the AFM data in Figure 2.2. The boundaries between the  $\approx 80$  nm diameter polycrystalline grains that are imaged in the phase contrast AFM image of Figure 2.2 are absent in the phase contrast AFM image in Figure 2.1. The symmetric  $\theta/2\theta$  X-ray diffraction data from the two heterostructures in Figure 2.3 demonstrate that the film grown on the un-doped CeO<sub>2</sub> template is oriented with its (001) orientation normal to the surface, as is the thin single crystal (001) template. In contrast, the grains in the polycrystalline GDC film grown directly on the sapphire substrate are primarily oriented with their (111) direction normal to the surface with a smaller volume fraction of the grains assuming an (001) orientation. X-ray diffraction  $\phi$ -scans probes the in-plane orientation of a film by recording the azimuthal angle ( $\phi$ ) at which crystallographic planes whose normal are inclined to the surface occur. The  $\phi$ -scan data shown in Figure 2.4 recorded from the (001)-oriented GDC film demonstrates that the film is indeed single crystal. This is confirmed by the presence of four well-defined peaks from the (204) planes of the film separated by  $90^\circ$ , as would be expected from a single crystal (001)-oriented GDC film. The (001) GDC film is therefore confirmed as being single crystal with a single domain of in-plane crystallographic orientation. There are no grain boundaries in this film. In contrast,  $\phi$ -scans recorded from the (111) oriented film for which the AFM phase contrast data indicated boundaries between  $\approx 80$  nm grains showed no

evidence of well-defined peaks at specific azimuthal angles. The intensity was weak and independent of azimuthal angle  $\phi$ , indicating that the polycrystalline film consisting of grains whose orientation is predominately (111) in the direction normal to the interface exhibit a random in-plane orientation: The film grown directly on the sapphire substrate is polycrystalline with a fiber texture (consisting of grains with a strongly preferred orientation in one direction and a random orientation in the other two directions). The relatively narrow full-width-at-half-maximum (FWHM) of the x-ray diffraction (002) rocking curve data (FWHM =  $0.37^\circ$ ) recorded from the single crystal (001) GDC film shown in Figure 2.5 is taken as evidence of excellent crystalline quality in that the narrowest rocking curve data that the authors have found reported in the literature [21] for epitaxial GDC films grown on other substrates had a FWHM =  $0.6^\circ$ . The broader FWHM ( $1.76^\circ$ ) of the (111) rocking curve data recorded from the polycrystalline film in Figure 2.5 is a measure of the angular distribution of the grain orientations. This breadth, though of course broader than that of the single crystal film, indicates a very strong fiber texturing of the polycrystalline film. The AFM data recorded from both films indicate a surface roughness (RMS) less than 1% of the film thickness, indicating that these films are well within the criteria for a homogeneous film for assuring the accuracy in Van der Pauw measurements of the conductivity. The relative intensity of the Gd peak and the Ce peaks in Energy dispersive spectroscopy (EDS) data recorded in an electron microscope did not vary significantly between the two samples, indicating that the Gd content of the two films



are equivalent. Though quantitative interpretation of the the EDS data is difficult, it appears as if the Gd concentration in both films is approximately 2 to 3 times the composition of the target, a deposition-condition-dependent difference between film and target composition that has been reported by other researchers [22] who have deposited GDC films by RF sputtering. Spectrally resolved optical reflectance measurements demonstrate that the two films have thicknesses that agree to within 3%. In short, as expected from employing identical growth conditions, the two films are largely identical except for the presence of boundaries between 80 nm grains in one film that are not present in the other film.

The measured conductivity vs temperature data for the single crystal GDC film are summarized in Table 2.1, and that for the polycrystalline film is summarized in Table 2.2. The two sets of  $\ln(\sigma T)$  vs  $1/T$  data are plotted in Figure 2.6 and are characterized by a slope and intercept from which an activation energy for the conduction mechanism can be extracted. These data are reported in Table 2.3. The precision resulting from using 336 measurements to characterize the temperature-dependent conductivity of single crystal and polycrystalline GDC is reflected in the high linearity of the two sets of  $\ln(\sigma T)$  vs  $1/T$  data. This is seen by inspection of the R-values very close to 1, the low standard error in the y-estimate of the regression, and the low uncertainties in the extracted values of the intercept and slope in Table 2.3. Conductivity values for the polycrystalline film are lower than those of the single crystal film by a factor of 4 at the higher temperatures, and by more than an order of magnitude

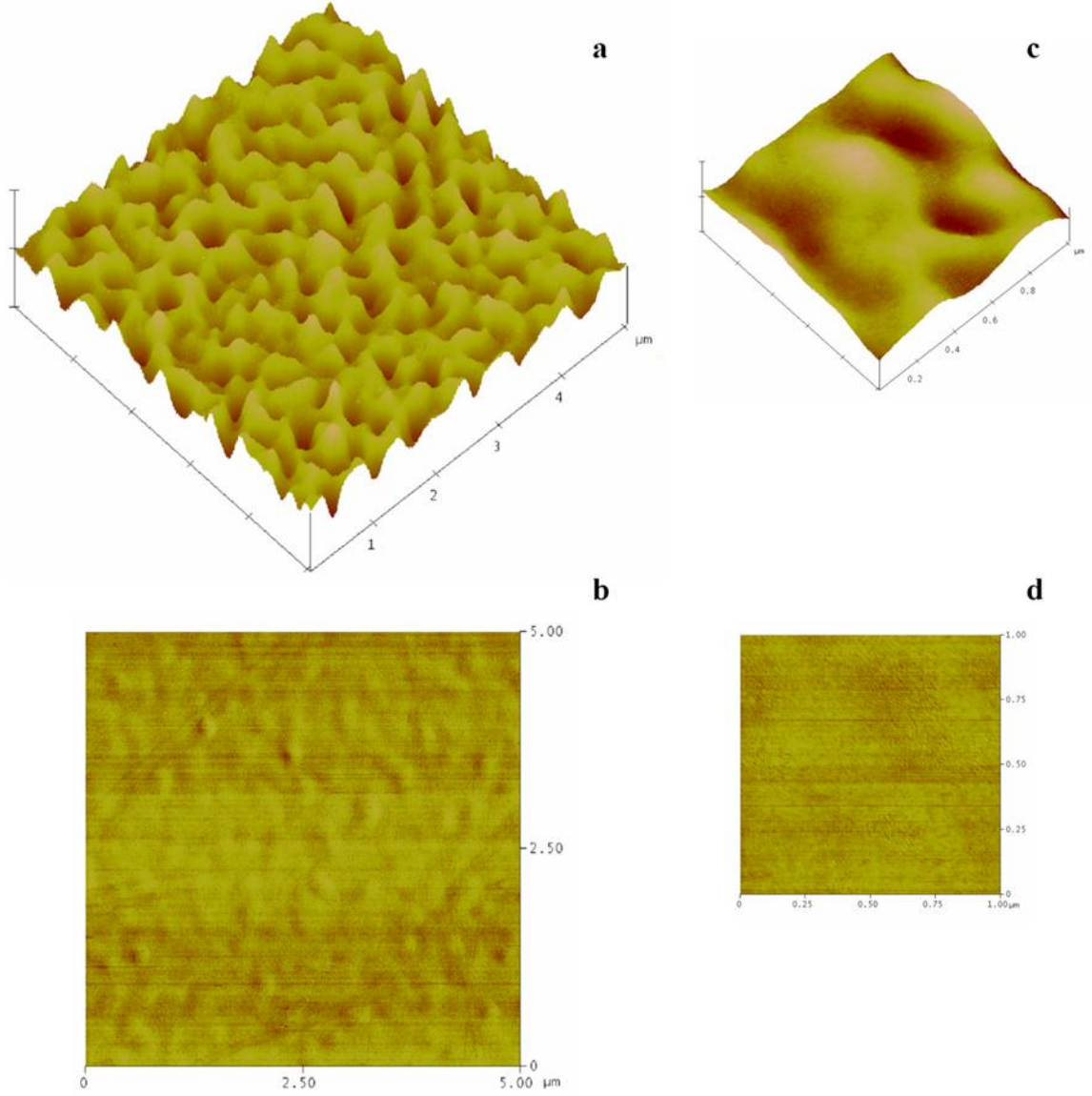


**Figure 2.1:** The surface morphology of the  $\approx 300$  nm (001)-oriented single-crystal GDC film grown on the single crystal  $\text{CeO}_2$ -buffered r-plane sapphire substrate. a)  $5 \times 5 \mu\text{m}$  3D height image with y axis increment = 12 nm/div. b)  $5 \times 5 \mu\text{m}$  phase contrast image c)  $1 \times 1 \mu\text{m}$  3D height image data with y axis increment = 12 nm/div d)  $1 \times 1 \mu\text{m}$  phase-contrast image. No grain boundaries are apparent in the single-crystal film.

at the lower temperatures. The activation energies extracted from the  $\ln(\sigma T)$  vs.  $1/T$  data for the single crystal and polycrystalline GDC thin films are  $0.85 \pm 0.01$  eV and  $0.99 \pm 0.01$  eV, respectively. The larger activation energy for the polycrystalline film as

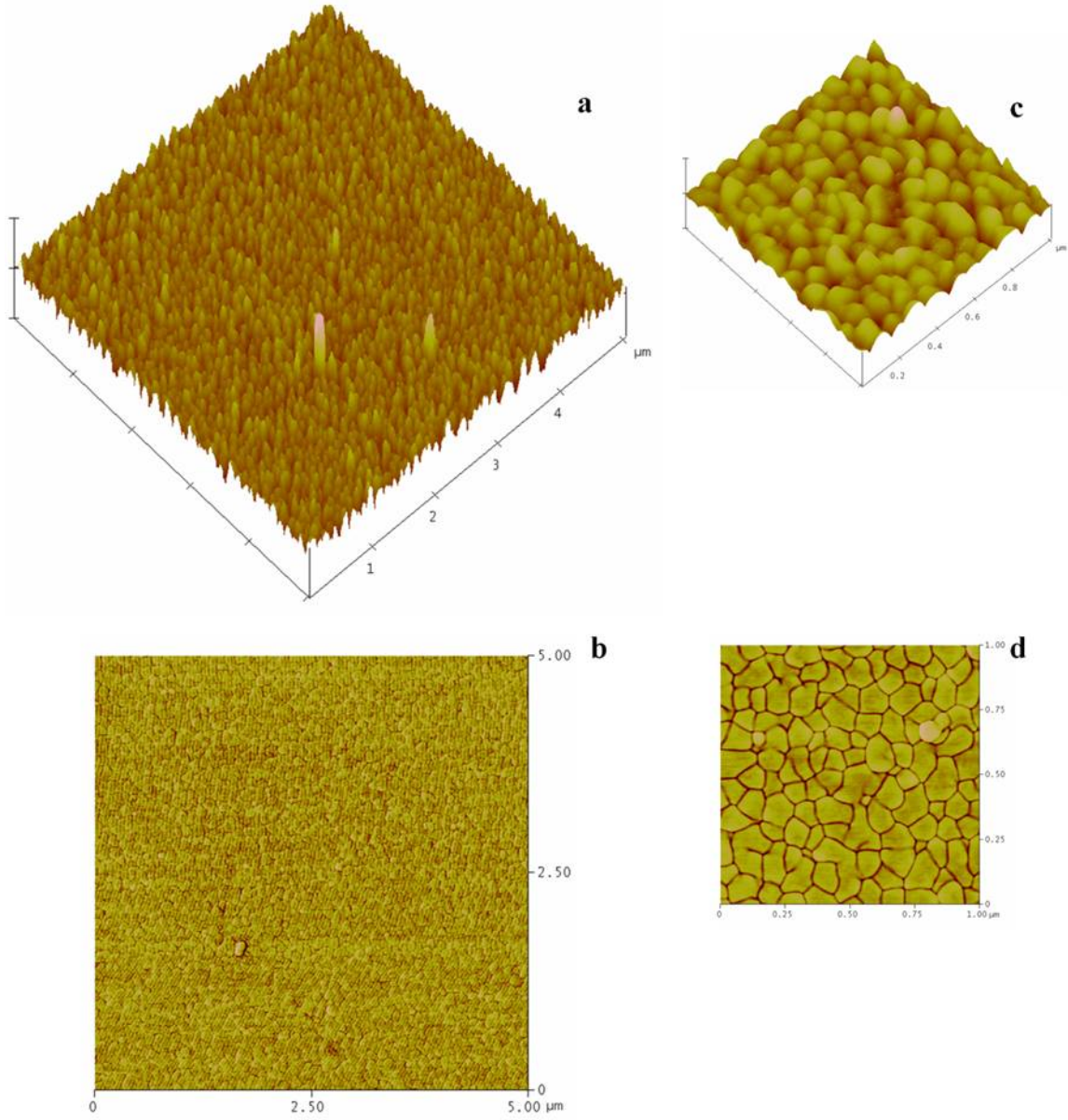


**Figure 2.2:** The surface morphology of the  $\approx 300$  nm thick highly oriented (111) polycrystalline GDC films grown on as received r-plane sapphire substrate. a)  $5 \times 5 \mu\text{m}$  3D height image with y axis increment = 12 nm/div. b)  $5 \times 5 \mu\text{m}$  phase contrast image c)  $1 \times 1 \mu\text{m}$  3D height image data with y axis increment = 12 nm/div d)  $1 \times 1 \mu\text{m}$  phase-contrast image. The polycrystalline film consists of sub-micron grains.

compared to the single-crystal film is consistent with a carrier mobility reduced by an increased potential energy barrier for charge carrier transport due to having to cross

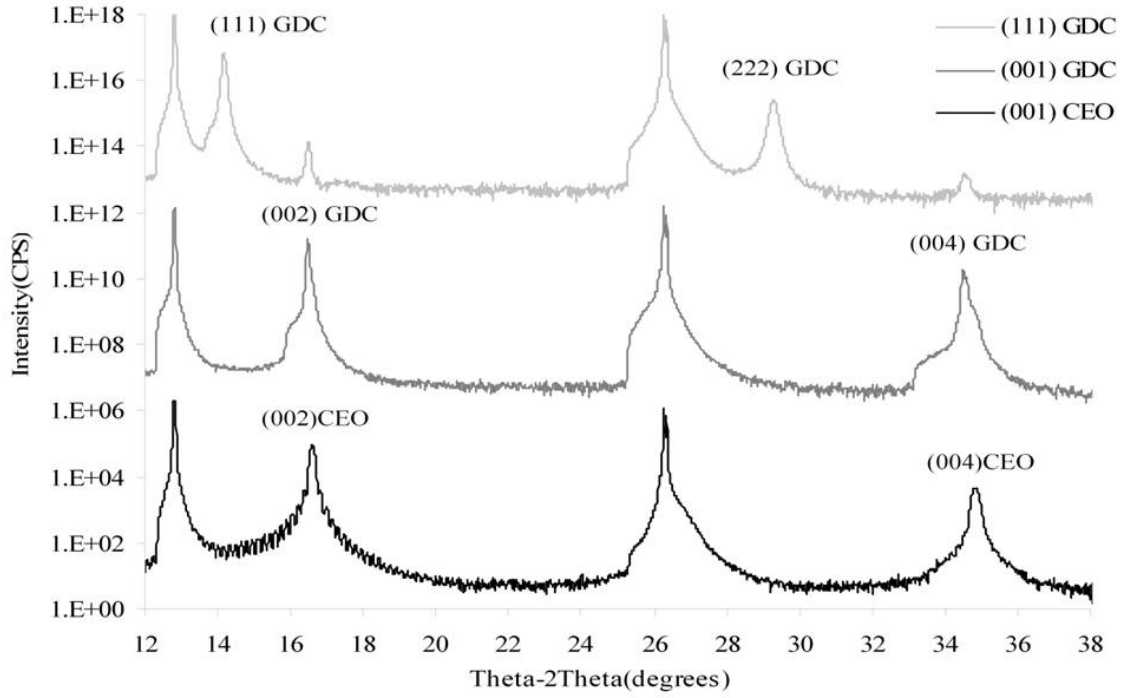


**Figure 2.3:** Comparison of  $\theta/2\theta$  XRD data from the  $\approx 300$  nm GDC film grown on the as-received  $\text{Al}_2\text{O}_3$  substrate (denoted as "(111) GDC"), with the data for the  $\approx 300$  nm GDC film grown on the un-doped 38 nm  $\text{CeO}_2$ -buffered substrate (denoted "(001) GDC") and the data recorded from a the 35 nm single-crystal (001)  $\text{CeO}_2$  buffer layer with no subsequent GDC growth (denoted as "(001) CEO"). The GDC grown on the as-received sapphire is of mixed orientation, with most of the film consisting of (111)-oriented material where the GDC grown on the buffered substrate consists entirely of material with a (001) orientation.

a boundary between  $\approx 80$  nm diameter single crystal regions in the polycrystalline GDC. These data clearly demonstrate that the boundaries separating  $\approx 80$  nm grains degrade the conductivity of GDC films in the temperature regime between 400 and 700°C.

Single crystal GDC films have been shown here to be more conductive than the polycrystalline films over the temperature range of 400-700°C. The  $\ln(\sigma T)$  vs  $1/T$

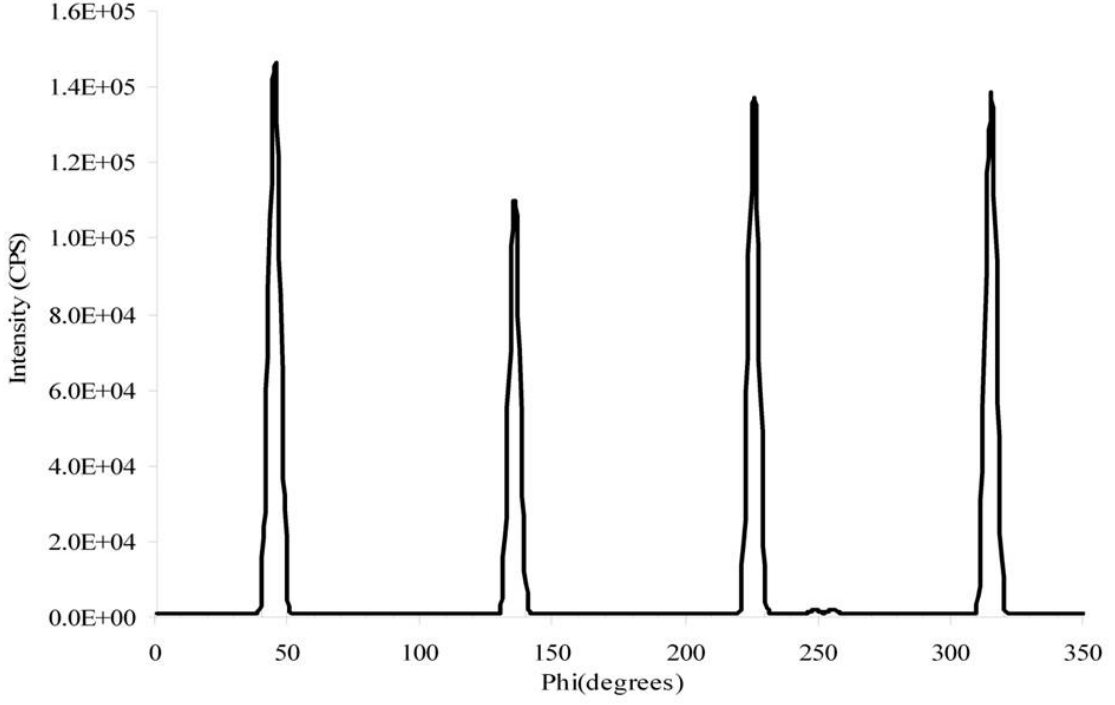


**Figure 2.4:** XRD  $\phi$ - scan data for the  $\approx 300$  nm (001) GDC grown on the buffered sapphire substrate. The 4-fold symmetry of the asymmetric (204) GDC peaks shows the in-plane epitaxial relationship between the GDC film and the sapphire substrate and demonstrates that the (001) GDC film is single-crystal.

**Table 2.1:** Single crystal (001)-oriented GDC without grain boundaries: Summary of data used to calculate the temperature dependent conductivity.

| Temp<br>(°C) | 1000/T<br>(K <sup>-1</sup> ) | I<br>(nA) | RSheet<br>( $\Omega/\square$ ) | $\rho$<br>( $\Omega\text{-cm}$ ) | $\Sigma$<br>( $\Omega\text{-cm}$ ) <sup>-1</sup> | Ln( $\sigma T$ )  |
|--------------|------------------------------|-----------|--------------------------------|----------------------------------|--|-------------------|
| 702          | 1.03                         | 50        | 8.467E5 $\pm$ 7E2              | 24.0 $\pm$ 0.2                   | 4.16E2 $\pm$ 3E4                                 | 3.703 $\pm$ .007  |
| 650          | 1.08                         | 50        | 1.406E6 $\pm$ 2E3              | 39.9 $\pm$ 0.3                   | 2.50E2 $\pm$ 2E4                                 | 3.141 $\pm$ .007  |
| 598          | 1.15                         | 50        | 2.454E6 $\pm$ 1E3              | 69.7 $\pm$ 0.5                   | 1.43E2 $\pm$ 1E4                                 | 2.526 $\pm$ .007  |
| 544          | 1.22                         | 50        | 4.6961E6 $\pm$ 7E3             | 133.4 $\pm$ 0.9                  | 7.50E3 $\pm$ 5E5                                 | 1.813 $\pm$ .007  |
| 487          | 1.32                         | 50        | 1.0681E7 $\pm$ 7E3             | 303 $\pm$ 2                      | 3.30E3 $\pm$ 2E5                                 | 0.919 $\pm$ .007  |
| 433          | 1.42                         | 10        | 2.747E7 $\pm$ 4E4              | 780 $\pm$ 6                      | 1.28E3 $\pm$ 1E5                                 | -0.100 $\pm$ .007 |
| 378          | 1.54                         | 10        | 8.636E7 $\pm$ 1E4              | 2450 $\pm$ 20                    | 4.08E4 $\pm$ 3E6                                 | -1.326 $\pm$ .007 |

data from these two films are compared to those reported in the literature [1, 3, 15, 17, 21, 23] for high conductivity thin-film GDC measured between 400 and 700°C in Table 2.4 and Figure 2.7. The comparison demonstrates that the single crystal film

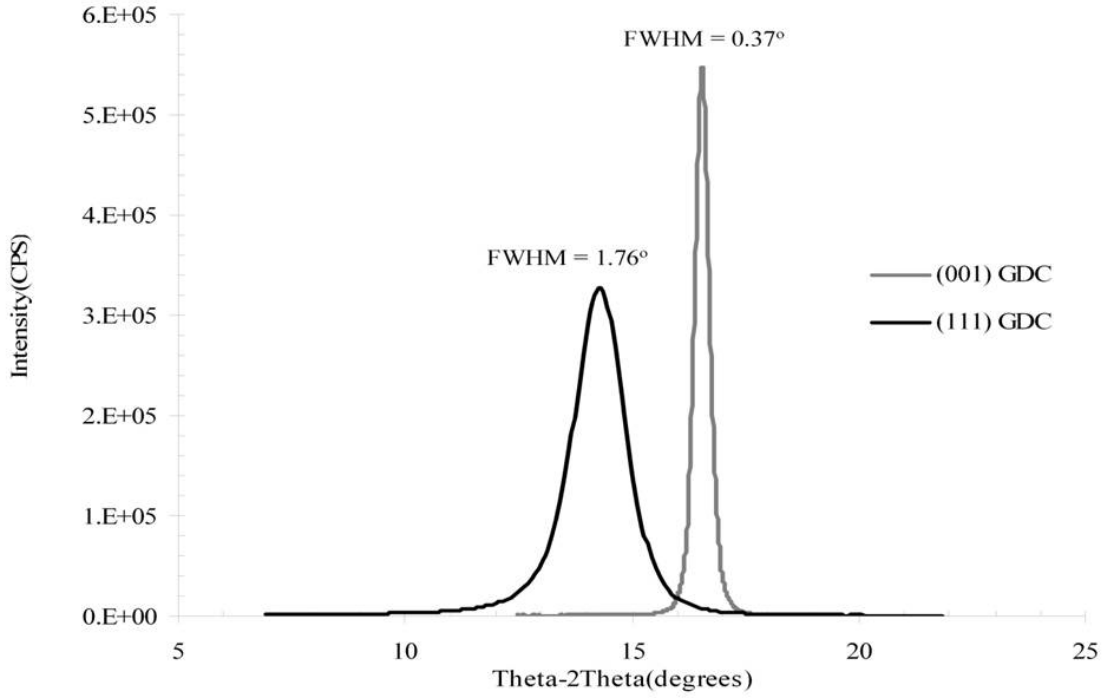


**Figure 2.5:** a) Rocking curve of (111) peak of highly oriented polycrystalline GDC with  $\approx 300$  nm thickness and b) Rocking curve of (002) plane of the epitaxial GDC film. Scans were done with count time = 2, step size =  $0.05^\circ$  for (111) GDC. The lower step size =  $0.015^\circ$  is used for (002) GDC at the same count rate.

**Table 2.2:** Polycrystalline (111)-oriented GDC with sub-micron grains: Summary of data used to calculate the temperature dependent conductivity.

| Temp<br>( $^\circ\text{C}$ ) | 1000/T<br>( $\text{K}^{-1}$ ) | I<br>(nA) | RSheet<br>( $\Omega/\square$ )   | $\rho$<br>( $\Omega\text{-cm}$ ) | $\sigma$<br>( $\Omega\text{-cm}$ ) $^{-1}$ | $\text{Ln}(\sigma T)$ |
|------------------------------|-------------------------------|-----------|----------------------------------|----------------------------------|--|-----------------------|
| 699                          | 1.03                          | 500       | $2.0976\text{E}6 \pm 7\text{E}2$ | $61.7 \pm 0.4$                   | $1.62\text{E}2 \pm 1\text{E}4$             | $2.756 \pm .007$      |
| 647                          | 1.09                          | 200       | $3.8333\text{E}6 \pm 7\text{E}2$ | $112.7 \pm 0.8$                  | $8.87\text{E}3 \pm 6\text{E}5$             | $2.097 \pm .007$      |
| 594                          | 1.15                          | 50        | $7.580\text{E}6 \pm 1\text{E}3$  | $223 \pm 2$                      | $4.49\text{E}3 \pm 3\text{E}5$             | $1.361 \pm .007$      |
| 540                          | 1.23                          | 50        | $1.700\text{E}7 \pm 2\text{E}4$  | $500 \pm 4$                      | $2.00\text{E}3 \pm 1\text{E}5$             | $0.487 \pm .007$      |
| 487                          | 1.32                          | 50        | $4.222\text{E}7 \pm 1\text{E}4$  | $1241 \pm 8$                     | $8.06\text{E}4 \pm 5\text{E}6$             | $-0.494 \pm .007$     |
| 432                          | 1.42                          | 10        | $1.3102\text{E}8 \pm 7\text{E}4$ | $3850 \pm 30$                    | $2.60\text{E}4 \pm 2\text{E}6$             | $-1.699 \pm .007$     |
| 377                          | 1.54                          | 10        | $4.6949\text{E}8 \pm 3\text{E}4$ | $13,800 \pm 90$                  | $7.24\text{E}5 \pm 5\text{E}7$             | $-3.057 \pm .007$     |

exhibits conductivities in this temperature regime that are as high or higher than any of the films that have reported conductivity enhancements due to the presence of sub-micron grains in this temperature range (Figure 2.7). The  $\ln(\sigma T)$  vs  $1/T$  data

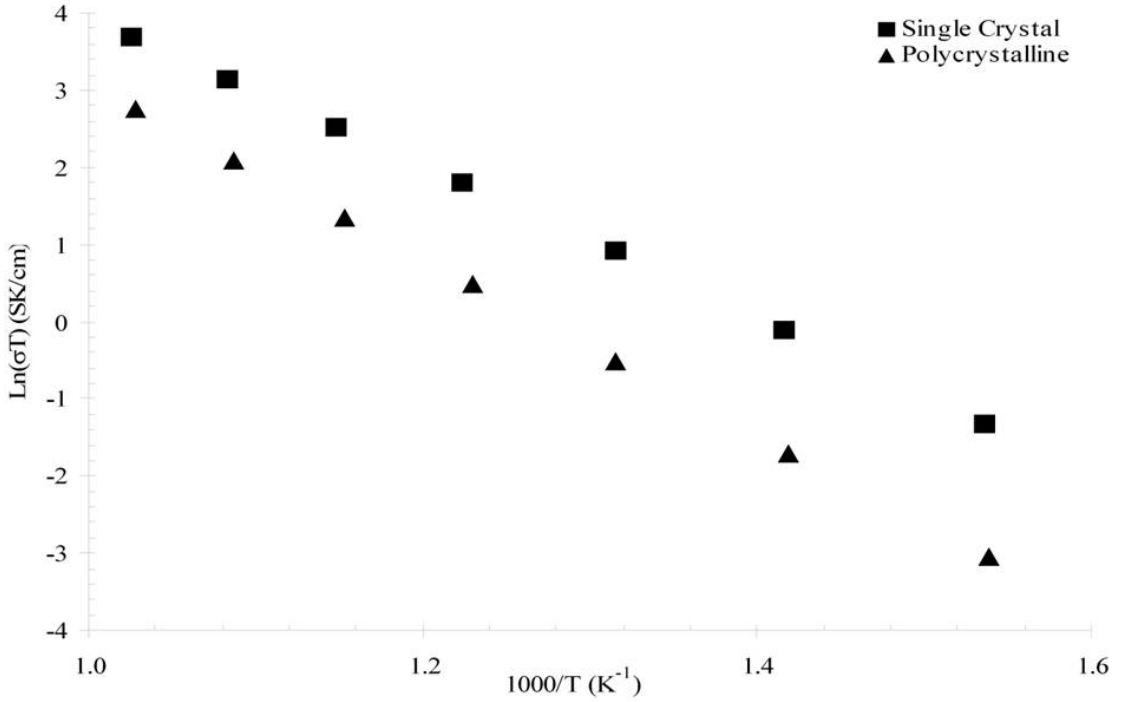


**Figure 2.6:** The plot of  $\ln(\sigma T)$  as a function of  $1000/T$  of (111) GDC polycrystalline film with boundaries separating submicron grains and (001) epitaxial film with no grain boundaries. The presence of the grain boundaries significantly reduces the ionic conductivity of GDC over the entire temperature range.

**Table 2.3:** Polycrystalline (111)-oriented GDC with sub-micron grains: Summary of data used to calculate the temperature dependent conductivity.

| Film                     | (-)Slope<br>( $\times 10^{-3} \text{K}$ ) | Intercept        | R-Factor | Std error<br>in $\ln(\sigma T)$ | $\Delta H_m$    |
|--------------------------|---|------------------|----------|---------------------------------|-----------------|
| Polycrystalline(111) GDC | $11.43 \pm 0.03$                          | $14.53 \pm 0.08$ | 0.9998   | 0.03                            | $0.99 \pm 0.01$ |
| Single crystal(001) GDC  | $9.83 \pm 0.007$                          | $13.80 \pm 0.09$ | 0.9997   | 0.03                            | $0.85 \pm 0.01$ |

recorded from the single crystal GDC grown here is in very close agreement with that recorded for single crystal GDC in the study by Chen et al. [1]. This further confirms our results of higher conductivity in single crystal GDC than polycrystalline in the 400-700°C temperature range.

**Table 2.4:** A comparison of GDC  $\ln(\sigma T)$  vs  $(1/T)$  data for thin film GDC in the literature. Activation energy ( $E_a$ ), conductivity ( $\sigma$ ), and the Y-intercept ( $\ln(\sigma T)$ ), were extracted by analyzing published plots of literature data.

| Ref.       | %Gd  | Crystallinity | Grain Size<br>(nm) | Thickness<br>(nm) | Growth technique/<br>Temp. | $E_a$<br>(eV) | $\ln(\sigma T)$ |
|------------|------|---------------|--------------------|-------------------|----------------------------|---------------|-----------------|
| Joo [23]   | 21   | (111) poly.   | 40                 | -                 | PLD 700°C                  | 0.83          | 13.17           |
| Bera [17]  | 19.2 | (111) poly.   | 8                  | 180               | MBE 652°C                  | 0.91          | 14.71           |
| Bera [17]  | 8.4  | (111) poly.   | 8                  | 180               | MBE 652°C                  | 0.86          | 13.27           |
| Chen [1]   | 20   | epi.          | -                  | 300               | PLD 830°C                  | 0.86          | 14.04           |
| Chen [1]   | 20   | epi.          | -                  | 300               | PLD 830°C                  | 0.82          | 12.95           |
| Suzuki [3] | 20   | rand. poly.   | 36                 | 110-630           | Spin coating               | 1.3           | 15.81           |
| Suzuki [3] | 20   | rand. poly.   | 9                  | 110-630           | Spin coating               | 1.02          | 13.74           |
| Rupp [15]  | 20   | rand. poly.   | 65                 | 500-800           | PLD room temp.             | 0.98          | 13.83           |
| Rupp [15]  | 20   | rand. poly.   | 78                 | 300-400           | Spray pyrolysis            | 0.97          | 14.09           |

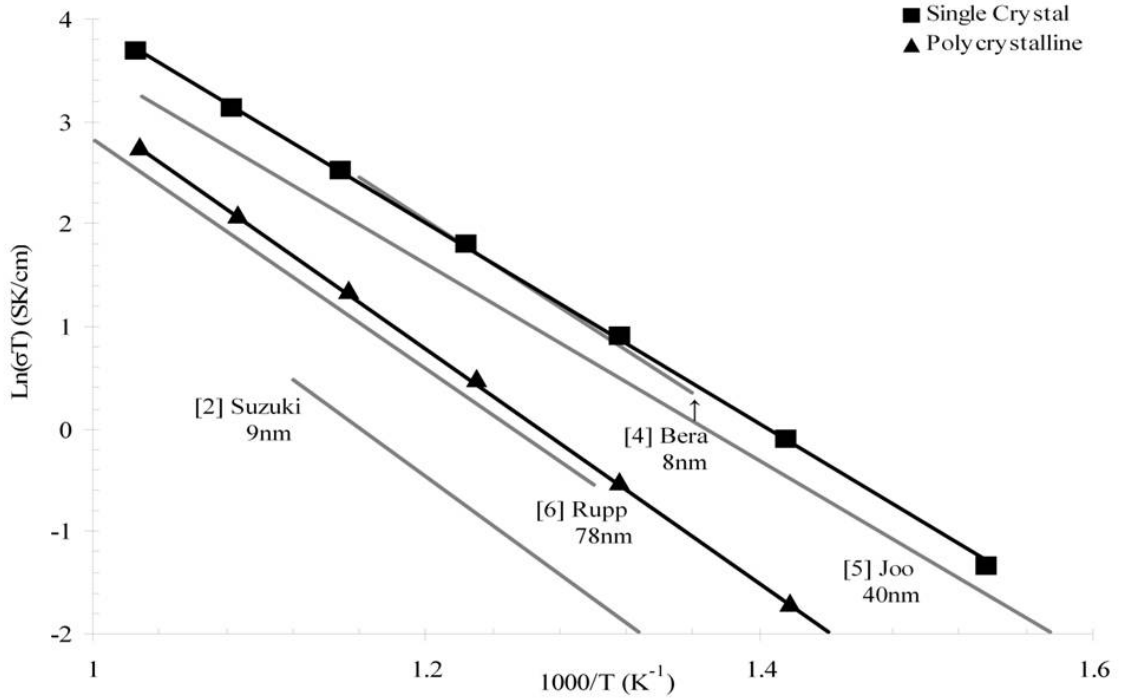


**Figure 2.7:** The total conductivity of submicron grained GDC samples as a function of a reciprocal of temperature ( $T$ ) $\times 1000$  for the highest published data sets collected in the 400-700°C range. Values given under the researchers name provide the reported grain size for each data set. Epitaxial, single crystal GDC data provided by Chen et al. [1] aligns almost identically with the single crystal data from this study, but were not included in the plot for clarity.



The data reported here does not rule out the potential for an enhancement of ionic conductivity in GDC due to grain sizes much smaller than 80 nm. A broader review of published  $\ln(\sigma T)$  vs  $1/T$  data for both thin-film and bulk oxide electrolytes in the literature, including data taken in temperature ranges other than the 400-700°C range studied in this work, shows trends of decreasing ionic conductivity with decreasing grain size for grains that are tenths of a micron or larger [24–27] and increases in ionic conductivity with decreasing grain size for grains that are in the nanometer range [2–4, 18]. If these differences are not due to changes in the GDC other than the grain size, the trends would suggest that multiple mechanisms for ionic transport may be present and that the dominate mechanism may change as a function of grain size. If the resistance to ionic motion were to be highest when crossing a grain boundary, lower when traveling through the bulk, and lowest when traveling along a grain boundary, the different dependencies of the volume fraction of each path on grain size could explain the changing behavior [10] of the conductivity versus grain size relationship found in the literature. For example, inspection of Figure 2.7 shows that if the data from Suzuki et al. are excluded, there would appear to be a trend suggesting that when grain sizes are reduced to  $\approx 10$  nm, the reduction in ionic mobility due to ions having to cross grain boundaries is offset by an increase in ionic mobility due to ions traveling along grain boundaries. The high ionic conductivities observed for single crystal GDC films reported here along with the potential for the Gd-content in the films to change with changes in deposition conditions that

are intended to only change grain size indicates that such a hypothesis can only be rigorously tested through a systematic comparison of data taken from single crystal and fine-grained GDC films that, though grown under identical conditions, possess quantifiable differences in volume fractions of the intra-grain, across-grain-boundary, and along-grain-boundary ionic conduction paths. Sets of  $\ln(\sigma T)$  vs  $1/T$  data taken from single-crystal and polycrystalline GDC films grown with different grain sizes by the methods described above would be one approach to obtain such a data set. Work is underway to make and analyze these measurements.

## 2.5 Conclusions

In summary, methods have been developed to grow GDC films on sapphire substrates that are largely identical except for the presence of boundaries separating 80 nm diameter grains or the complete absence of grain boundaries. Conductivity data recorded in the temperature range of 400-700°C indicate that the ionic conductivity of the single crystal GDC film in this temperature range is as high or higher than high-conductivity polycrystalline GDC films studied in the literature whose large ionic conductivity was attributed to the presence of sub-micron grains. The mobility of the charge carriers was significantly reduced in the polycrystalline sample over all temperatures, leading to a reduction in the conductivity over the entire temperature range. Direct comparison of the conductivity vs. temperature data for single crystal

and polycrystalline GDC thin films showed that the presence of boundaries separating  $\approx 80$  nm diameter grains does not enhance, but rather reduces the in-plane ionic conductivity of the GDC film.

\*

---

\*Reprinted from Solid State Ionics, Vol 181, M. Swanson, N. Tangtrakarn, M. Sunder, and P.D. Moran, Impact of the presence of grain boundaries on the in-plane ionic conductivity of thin film Gd-doped CeO<sub>2</sub>, 379-385, 2010, with permission from Elsevier.

## Chapter 3

# Impact of the surface/interface on the ionic conductivity of thin film Gd-doped $\text{CeO}_2$

Authors: Matthew Swanson, Madhana Sunder, Natee Tangtrakarn, Lakshmi Krishna,  
and P.D. Moran

\*

---

\*The material contained in this chapter has been submitted to the journal *Solid State Ionics*.

### 3.1 Abstract

Literature reports suggest that the surface and interface regions of thin film Gd-doped CeO<sub>2</sub> (GDC) may act as highly conductive paths for ionic transport [2, 28]. However, no study has been published that directly tests the impact of the surface and interface on the total ionic conductivity of single crystal thin film GDC. In this study, single crystal GDC films have been grown to thicknesses varying from 20 to 500 nm and their conductivities have been measured in the 500-700°C temperature range. Decreasing conductivity with decreasing film thickness was observed. Analysis of the conductivity data is consistent with the presence of an approximately 50 nm layer of less conductive material in every film. This study concludes that the surface and interface regions of thin film GDC are less conductive than the bulk single crystal regions, rather than being highly conductive paths.

Keywords: GDC, Thin film, Single crystal, Interface conductivity

### 3.2 Introduction

The ionic conductivity of a Gadolinium doped Ceria (GDC) film surface and interface at temperatures between 500-700°C is of interest [2, 3, 10, 21, 22, 28] due to the application of the material as an electrolyte for intermediate temperature Solid Oxide

Fuel Cells (SOFCs). Though little work has been performed to determine the effect of a film surface and interface on the conductivity of a GDC film, the effects of grain boundary interfaces on the conductivity of GDC have been studied by numerous groups [10, 29–33]. These studies have come to the following conclusions as to the role of grain boundaries: grain boundaries are less conductive than the bulk [10, 29], they approach the conductivity of the bulk for dopant concentrations above 15% [30–32], and they are a smaller component of the total conductivity at higher temperatures [10, 33]. Furthermore, recent results [2–4] have shown a trend of increasing ionic conductivity in GDC with decreasing grain size. However, even with the conductivity enhancement, polycrystalline GDC with an approximately 80 nm grain size is still a factor of at least 4 less conductive than single crystal GDC over the 400-700°C temperature range [9].

Efforts to further understand the effects of grain boundaries on the ionic conductivity of GDC have turned researchers [9, 21, 34] towards the investigation of single crystal GDC. These studies have provided insight into the effects of grain boundaries on the ionic conductivity of GDC, but none of the studies have investigated the effects of the surface or interface on the conductivity of GDC. It has been asserted in the literature that the exceptionally high ionic conductivity observed in thin GDC films is due to the surface or substrate/film interface acting as a high conductivity path for ions [2, 28]. Those studies were not performed on single crystal GDC and, therefore, could not separate the impact of the ionic conduction along the surface and interface from

that along or across grain boundaries. A study to extract the surface and interface contributions to the total ionic conductivity of GDC single crystal films would resolve this question, but is absent from the literature. This work addresses the need for such an analysis.

In this work, the impact of the GDC film surface and interface on the in-plane ionic conductivity of GDC films is examined. Though a film's conductivity could be affected by the surface or interface, the remainder of this paper will refer to such contributions as interface effects for clarity. The approach to separate the impact of the film interface from the "bulk" and to isolate its contribution from that of grain boundaries is to fabricate a series of single-crystal GDC films of varying thickness on highly insulating r-plane  $\text{Al}_2\text{O}_3$  substrates and measure their conductivities over the 500-700°C temperature range. The conductivities are then directly compared to determine if a greater volume fraction of the interface region enhances or reduces the ionic conductivity of the films. The films' conductivity data are analyzed by plotting the conductance versus thickness. These data are analyzed to deduce the conductivity and the thickness of the interface region and that of the "bulk" region of the film.

### 3.3 Experimental Methods

The GDC films were grown on single crystal sapphire substrates using RF magnetron sputtering. An approximately 40 nm single crystal  $\text{CeO}_2$  buffer layer was first deposited on the sapphire substrates to promote the growth of single crystal GDC. A sputtering target with composition  $(10\%)\text{Gd}_2\text{O}_3(90\%)\text{CeO}_2$  was used along with deposition parameters that have previously resulted in single crystal GDC films. The details of the growth process were reported in earlier publications [9, 18]. All deposition parameters except growth time were held constant to ensure consistent composition between films. The growth time was varied over a factor of 20 to produce 5 films with thicknesses of 20, 44, 110, 278 and 500 nm.

The GDC thin films were structurally characterized using X-ray diffraction (XRD). XRD  $\phi$ -scans were used to determine the in-plane crystallographic orientation and to verify that the films were single crystal. XRD  $\theta/2\theta$  scans were used to determine the out-of-plane crystallographic orientation. The films were then diced into  $1\text{ cm}^2$  pieces for the conductivity measurements. Care was taken to cut all the films along the same directions in order to ensure that the in-plane orientation of the single crystal GDC films would be consistent during the conductivity measurements. Spectrally resolved optical reflectance was used on each  $1\text{ cm} \times 1\text{ cm}$  sample to determine the thickness accurately.



Conductivity data was recorded in air over the 500-700°C temperature range in 5°C intervals. The conductivity measurements were performed by painting opposite sides of the 1 cm<sup>2</sup> samples with platinum paste and connecting the conductive paste to the measurement equipment using platinum wires in a 4-wire bar geometry. Each sample's resulting data set consisted of approximately 50 conductivity versus temperature points. Conductivity data was taken for multiple samples at every film thickness and the data for each thickness group was found to agree within 3%. Only one data set was used from each film thickness in the final plots and analysis.

### 3.4 Results and Discussion

X-ray diffraction and spectrally resolved optical reflectance show all five films to be single crystals that differ in film thickness. Symmetric  $\theta/2\theta$  X-ray diffraction data, shown in Figure 3.1, demonstrates that the GDC films are oriented with the [001] direction normal to the surface, as is the thin single crystal [001] CeO<sub>2</sub> template. The  $\theta/2\theta$  data from the thickest film (500 nm) was used to calculate an out-of-plane lattice parameter of  $5.432 \pm 0.007 \text{ \AA}$ . This value agrees with the reported value of 5.428 [35] within the uncertainty of the measurement. The samples are expected to be fully dense from the epitaxial growth process used to make the films.  $\phi$ -scans showed four well-defined peaks from the asymmetric (204) planes indicating that the films have a single orientation in the plane of the film and are single crystals. The  $\phi$ -scan data

from the 500 nm film is shown in Figure 3.2. The azimuthal angle of the  $\phi$ -scans at which the peaks of the (204) planes occurred were used to orient the electrodes so that measurements were taken along the [110] direction in the GDC thin films. Spectrally resolved optical reflectance measurements of the films' thicknesses agreed closely with the expected values calculated from the growth times and previously measured growth rate. The uncertainty of  $\pm 3$  nm in the film thickness measurements dominate the uncertainty in the conductance data reported for the thinnest films.

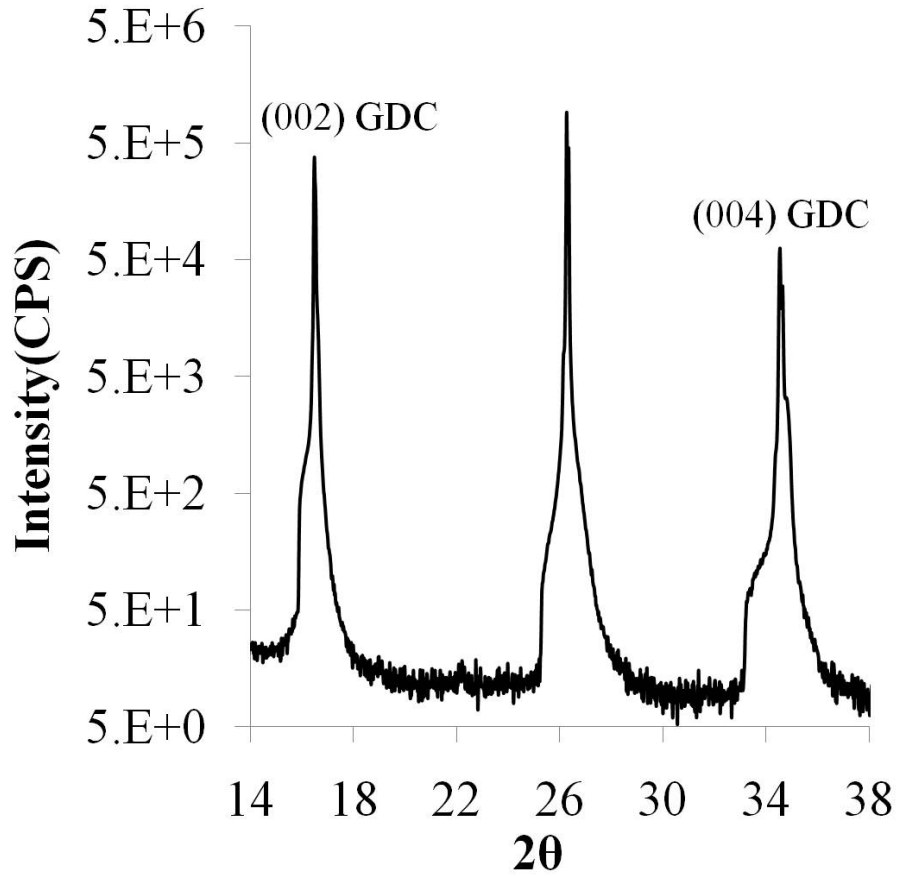


**Figure 3.1:** Symmetric  $\theta/2\theta$  X-ray diffraction data from the 500 nm GDC film showing the [001] out-of-plane orientation. The center peak is from the sapphire substrate.

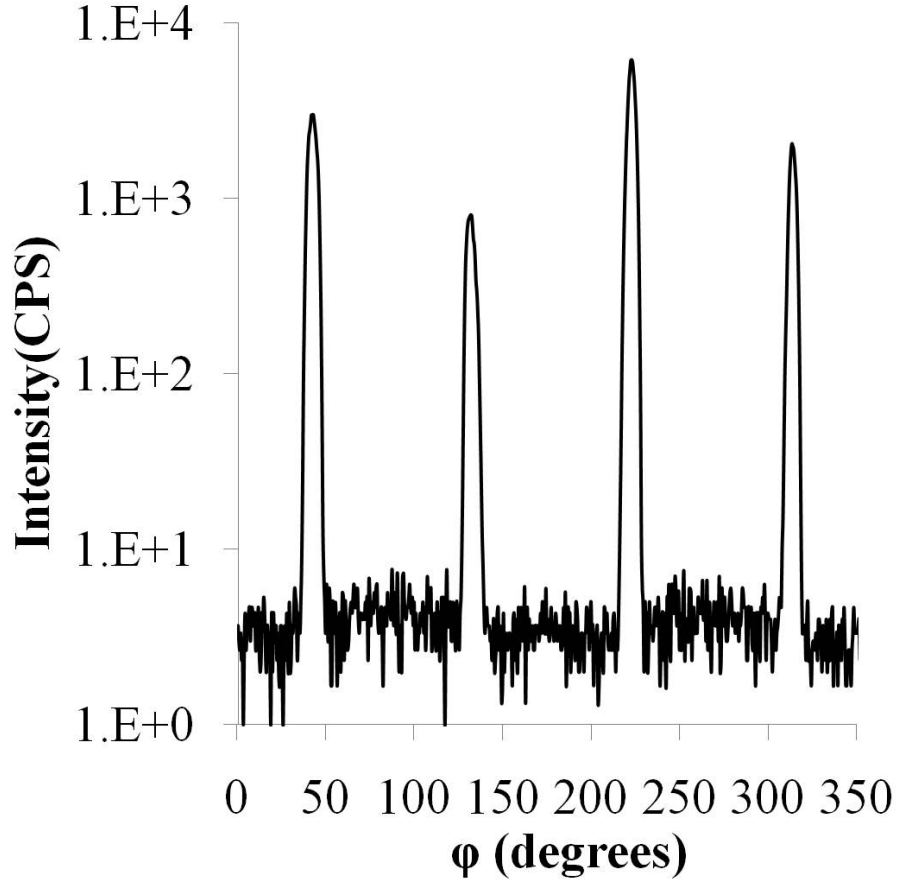


**Figure 3.2:** XRD  $\phi$ -scan data for the 500 nm (001) GDC film. The 4-fold symmetry of the asymmetric (204) GDC peaks shows that a single in-plane epitaxial relationship exists between the GDC film and the sapphire substrate demonstrating that the film is a single-crystal.

The measured conductivity vs temperature data collected for the five single crystal films are shown in an Arrhenius plot in Figure 3.3. The slope and intercept values from the Arrhenius plots have been extracted and the corresponding activation energies calculated. These data are reported in Table 3.1. The small uncertainties in the Arrhenius plot slope and intercept values as well as R values that are close to one reflect the precision of the data resulting from roughly 200 conductivity measurements. The data shows a clear trend of decreasing conductivity with decreasing film thick-

ness for the films that are 100 nm and thicker. The two films that have thicknesses less than 100 nm show a dramatic reduction in their conductivities as compared to those of the thicker films. The conductivities of these two thinnest films do not differ by more than the experimental uncertainty in the measurements. Conductivity measurements performed on samples consisting of only the undoped  $\text{CeO}_2$  confirmed that the conductance of the buffer layer was negligible compared to even the thinnest GDC film.

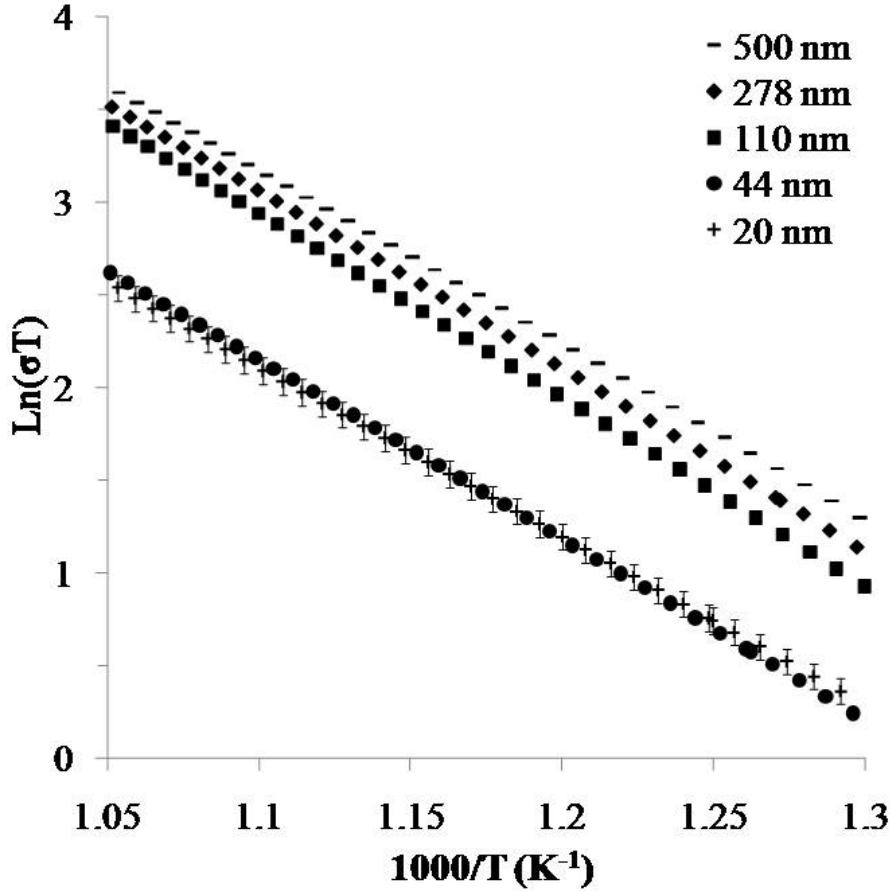


**Figure 3.3:** Arrhenius plot showing conductivity of five films of varying thickness. Uncertainties are less than the symbol size unless otherwise shown. The conductivities of the two thinnest films are dramatically reduced compared to those of the thicker films.

**Table 3.1:** Conductivity data for single crystal GDC films with varying thickness. The uncertainties represent 1 standard deviation in the fit of the data.

| Film Thickness<br>(nm) | (-)Slope        | Intercept        | R-Factor | $\Delta H_m$<br>(eV) |
|------------------------|-----------------|------------------|----------|----------------------|
| 500 $\pm$ 3            | 9.31 $\pm$ 0.02 | 13.41 $\pm$ 0.01 | 0.99985  | 0.80 $\pm$ 0.01      |
| 278 $\pm$ 3            | 9.57 $\pm$ 0.02 | 13.58 $\pm$ 0.02 | 0.99978  | 0.82 $\pm$ 0.01      |
| 110 $\pm$ 3            | 9.91 $\pm$ 0.02 | 13.84 $\pm$ 0.03 | 0.99982  | 0.85 $\pm$ 0.01      |
| 44 $\pm$ 3             | 9.68 $\pm$ 0.01 | 12.80 $\pm$ 0.05 | 0.99997  | 0.83 $\pm$ 0.01      |
| 20 $\pm$ 3             | 9.10 $\pm$ 0.06 | 12.02 $\pm$ 0.11 | 0.99998  | 0.78 $\pm$ 0.01      |

Inspection of Table 3.1 shows that there is a significant decrease in  $\ln(\sigma T)$ -intercept for the two thinnest films. The  $\ln(\sigma T)$ -intercept is a function of the carrier concentration. Its reduction indicates that the carrier concentration is lower for the two thinner films than the thicker films. The activation energies appear to be relatively constant over the range of thicknesses. The observed drop in conductivity for the thinnest films suggests that the interface has a significant effect on the conductivity of the films.

The reduction in the conductivity values for the two thinnest films motivates separation of the interface contribution from that of the "bulk" conduction in the films. The effect of the interface on the conductivity of the films can be observed by plotting the conductance versus thickness of the films at a set temperature. A schematic of this analysis is shown in Figure 3.4. If the line formed from this data passes through the origin then no interface effect is seen in the material. However, a line that passes above or below the origin indicates that the interface has a significant impact on the conductivity of the films. A line that passes above the origin indicates that the interface is a path of higher conductivity than that of the bulk and its intersection with the conductance axis can be used as an estimate for the conductance of the interface

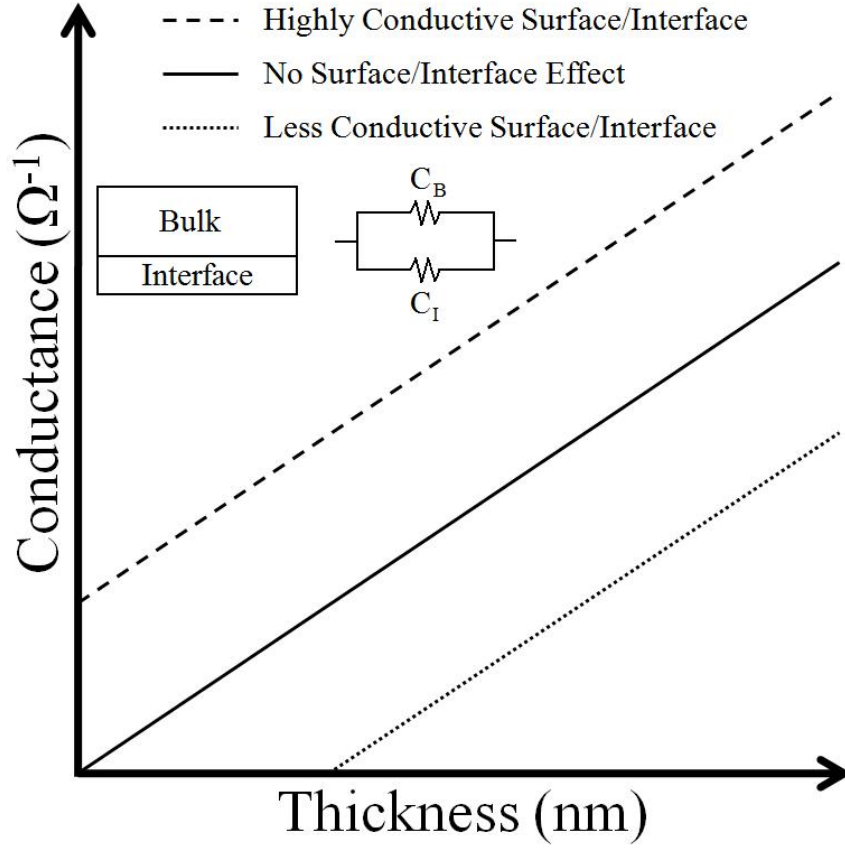


**Figure 3.4:** Schematic conductance versus thickness plot showing possible impacts of a film surface/interface. Figure inset shows bulk,  $C_B$ , and interface,  $C_I$  conductance paths in the two layer model.

layer. A line that passes below the origin indicates that the interface is a path of lesser conductivity than that of the bulk and the intersection with the thickness axis can be used as an estimate for the thickness of the layer of reduced conductivity. Furthermore, by modeling the interface and bulk contributions as distinct homogeneous layers (as shown in Figure 3.4 inset) one can solve for their specific conductivities and thicknesses using Equation 3.4.1.

$$C_T = C_B + C_I = \sigma_B * l_B + \sigma_I * l_I \quad (3.4.1)$$

Where  $C$ ,  $\sigma$ , and  $l$  are the conductance, conductivity, and thickness of the bulk,  $B$ , and interface,  $I$ , components of the total,  $T$  film. Conductance versus thickness plots have been produced using the five GDC films at 500°C and 700°C (Figures 3.5 and 3.6). These plots reveal the presence of a less conductive layer spanning about 50 nm in every sample. This layer appears to decrease slightly in thickness from 500°C to 700°C. Though only shown at 500°C and 700°C, this approximately 50 nm layer of reduced conductivity is observed in conductance versus thickness plots over the entire temperature range. The samples with a total thickness that is less than the 50 nm layer appear to consist entirely of this less conductive layer. The layer of reduced conductivity may be caused by reduction on the surface of the GDC films or by dopant segregation away from the surface. Though bulk reduction in GDC generally occurs at much lower oxygen partial pressures [8], significant surface reduction has recently been reported for GDC when exposed to air [36]. Segregation effects have been suggested to lead to a depletion in near-surface charge carriers [37]. A reduction in surface carrier concentration would be consistent with the reduction in  $\ln(\sigma T)$ -intercept observed for the two thinnest films. Another possible explanation for the less conductive layer would be diffusion of the Gd into the  $\text{CeO}_2$  buffer layer during the deposition. However, this is unlikely as the maximum temperature experienced by the films (850°C) is less than half GDCs melting point (2300°C) [38]. Additionally, diffusion of Gd to the buffer layer should occur to a greater extent in the thicker films that are held at the elevated temperature for up to 8 hours, while the thinner films

experience only 1 hour of the elevated temperature. This would have produced an apparent increase in the thickness of the less conductive layer with increasing total film thickness, but this effect was not observed in the conductivity data.

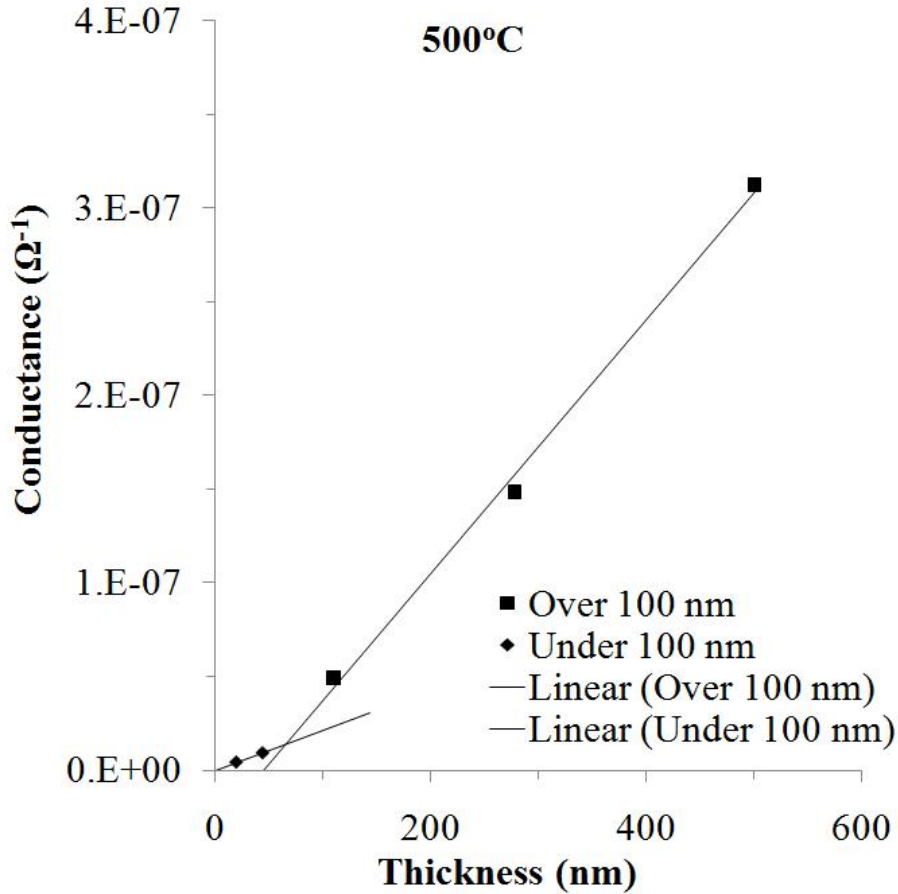


**Figure 3.5:** Conductance data for 5 single crystal GDC films at 500°C.

The conductance versus thickness data has been analyzed to extract an estimate of the interface and bulk conductivities from the total measured conductivity. The bulk conductivity was estimated using the conductance versus thickness slope and setting the intercept of the line to zero, as the middle line shows in Figure 3.4. This analysis was done using the conductance data in the 500 to 700°C temperature range for the



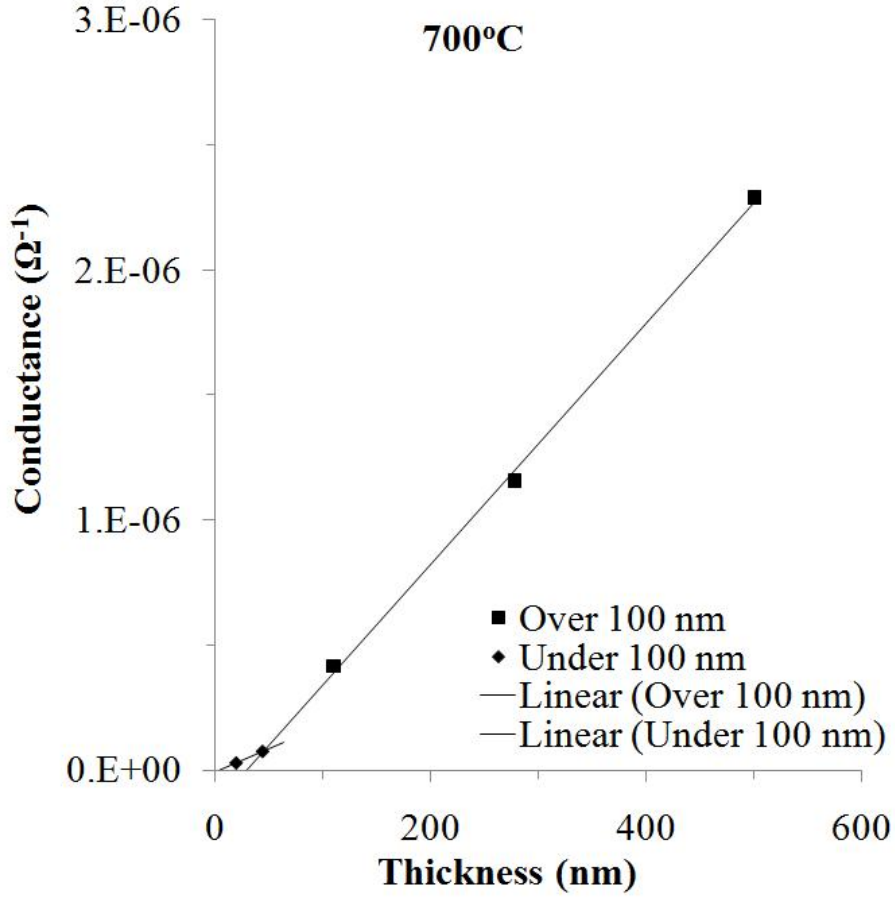


**Figure 3.6:** Conductance data for 5 single crystal GDC films at 700°C.

three films that were greater than 100 nm in thickness. The thinner films were not used as their thicknesses are smaller than the estimated thickness of the interface region. Theoretical bulk conductivity values were generated for each of the three film thicknesses and their values were averaged. The calculated bulk conductivity, bulk thickness and interface thickness values were used, along with the total conductance, to solve for the interface conductivity (Equation 3.4.1). The  $\ln(\sigma T)$ -intercepts and activation energies characterizing the bulk and interface conduction paths are given in Table 3.2. The  $\ln(\sigma T)$ -intercept and activation energy for the bulk path are close to

those obtained for the thickest film (500 nm) in this study and indicate that thicker films were probably not necessary for this study. A comparison between the bulk conductivity calculated in this study and the best conductivities for the ultrathin, nanocrystalline (20-50 nm) films reporting enhancement due to surface or interface conduction [2, 28] agree within  $\pm 10\%$  over the 500 to 700°C temperature range. Therefore, the observed conductivity increase was not a enhancement compared to the bulk GDC conductivity, but only compared to courser grained GDC films. This suggests that the conductivity enhancement may have been caused by the increased volume fraction of grain boundaries present in the films, but not due to the presence of a surface and interface. Similar reports of enhanced conductivity in nanocrystalline doped Ceria films have been reported by multiple groups in the literature [2–4, 13]. Although none of the data for the thinnest two films was used in the analysis, the surface/interface  $\ln(\sigma T)$ -intercept and activation energy values agree well with those of the thinnest films. This close agreement suggests that the thinnest films are made up entirely of the less conductive layer.

**Table 3.2:** Extracted  $\ln(\sigma T)$ -intercepts and activation energies characterizing the bulk and interface conduction paths. This data represents the average conductivity values calculated for the bulk and interface paths from the 110, 278, and 500 nm samples. The uncertainties represent 1 standard deviation in the fit of the data.

| Conduction Path | (-)Slope        | Intercept        | R-Factor | $\Delta H_m$<br>(eV) |
|-----------------|-----------------|------------------|----------|----------------------|
| Bulk            | $9.35 \pm 0.01$ | $13.51 \pm 0.06$ | 0.99999  | $0.82 \pm 0.02$      |
| Interface       | $9.46 \pm 0.01$ | $12.64 \pm 0.02$ | 0.99993  | $0.82 \pm 0.02$      |

The calculated bulk and interface components of the total conductivity for the 110,

278, and 500 nm films have been replotted on the Arrhenius plot shown in Figure 3.7. The two thinnest films were included for comparison, but no bulk component was calculated as their conductance values lie at or below the calculated thickness of the less conductive layer. The Arrhenius plot shows remarkable agreement between the calculated bulk components of all three thicker films. The calculated interface components of the thicker films exhibit the same reduction in conductivity as do the two thinner films. Again, none of the data from the thinner two films was used in the analysis that separated the bulk and interface conduction components. Therefore, this analysis could be used as a predictive tool to estimate the conductivity of very thin films as well as the impact of an interface on the total conductivity of thin films.

### 3.5 Conclusions

In summary, conductivity measurements have been performed on five single crystal GDC films in the 500 to 700°C temperature range that varied only by the thickness of the films. A clear trend of decreasing conductivity with decreasing film thickness was observed for the films larger than 100 nm. The two thinnest films had substantially reduced conductivity when compared to the thicker films. The measurements revealed that the combined impact of the film surface and film/substrate interface is to reduce the conductivity of the films. Analysis of the conductivity data suggests the presence of a layer of reduced conductivity spanning as much as 50 nm in all of the measured

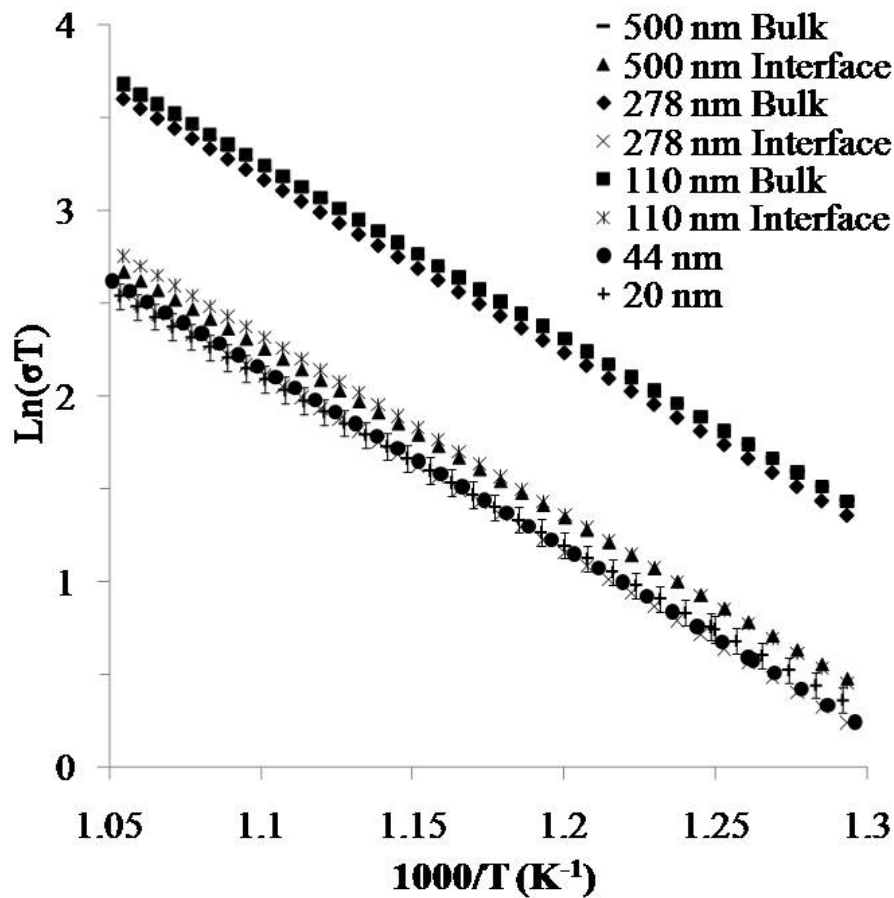


**Figure 3.7:** Arrhenius plot showing the bulk and interface components of the five GDC films. The data from the bulk component of the 500 nm film lies directly under the bulk component of the 110 nm film.

films. Further research is required to determine the cause and location of this less conductive layer.

## Chapter 4

# Impact of the crystallographic orientation on the ionic conductivity of thin film Gd-doped CeO<sub>2</sub>

Authors: Matthew Swanson and P.D. Moran

## 4.1 Abstract

This work investigates the ionic conductivity of thin film Gd-doped  $\text{CeO}_2$  (GDC) as a function of crystallographic orientation. A theoretical expression has been developed for the ionic conductivities of the [100] and [110] directions in single crystal GDC. This relationship is compared to experimental data collected from a single crystal GDC film. The film was grown to a thickness of  $\approx 300$  nm and its conductivity measured along the [100] and [110] orientations in the 500-700°C temperature range. The experimental data shows no statistically significant difference in the conductivities of the [100] and [110] directions in single crystal GDC. This result agrees with the theoretical model which predicts no difference between the conductivities of the two directions.

Keywords: GDC, Thin film, Single crystal, Crystallographic orientation

## 4.2 Introduction

Recently, the measurement and enhancement of the ionic conductivity of Gadolinium doped Ceria (GDC) has been an active area of research [2–9]. Research has been performed to analyze the effects of grain size [2–4], dopant type and concentration [5–8], and interfaces [9] on the ionic conductivity of the material. However,

no study has been performed to determine impact of the crystallographic orientation on the ionic conductivity of GDC. Such a study would require measurement of the ionic conductivity of single crystal samples along known crystallographic orientations and comparison of the measured conductivities to a theoretical model. This work addresses the need for such a study.

This work examines the impact of crystallographic orientation on the in-plane ionic conductivity of GDC films. The approach to determine the orientation dependence of the ionic conductivity is to develop a theoretical model and compare its result to experimental measurements. The approach to measure the orientation dependence of the ionic conductivity is to grow a single crystal GDC film on a highly insulating r-plane  $\text{Al}_2\text{O}_3$  substrate, characterize the film's in-plane orientation using X-ray diffraction, and measure the conductivity along two known crystallographic directions in the 500-700°C temperature range.

### 4.3 Experimental Methods

The GDC film used in this study was grown on a single crystal sapphire substrate using RF magnetron sputtering. The film was grown on an approximately 40 nm single crystal  $\text{CeO}_2$  buffer layer that was presputtered on the sapphire substrate to promote single crystal GDC growth. The GDC sputtering target had a composition

of (10%)Gd<sub>2</sub>O<sub>3</sub>(90%)CeO<sub>2</sub>. The growth process, which results in single crystal GDC films, has been reported in previous publications [9, 18].

X-ray diffraction was used to structurally characterize the GDC thin film. The in-plane crystallographic orientation and verification of the film’s single crystal nature was determined using a XRD  $\phi$ -scan. The out-of-plane crystallographic orientation was determined using a XRD  $\theta/2\theta$  scan. The film was then diced into 1 cm<sup>2</sup> samples. The samples were cut so that the edges were parallel to either the [100] or [110] crystallographic direction. In-plane conductivity measurements were performed using silver/platinum electrodes arranged in the 4-wire bar geometry. Measurements were taken in 5°C intervals over the 500-700°C temperature range. Details of the conductivity measurement setup, other than the electrode geometry, have been reported in a previous publication [9]. Spectrally resolved optical reflectance was used on each sample to determine the thickness.

## 4.4 Results and Discussion

The orientation dependence of the ionic conductivity can be determined theoretically by examining the flux across a plane for each orientation. The well known formula [39] for expressing the flux of ions,  $\mathbf{F}_{[hkl]}$ , across a plane due to an electric field is shown in Equation 4.4.1.



$$F_{[hkl]}^{\vec{}} = \frac{\beta}{C_N} n_{hkl} N_v (1 - N_v) \nu_o \Delta \vec{P}_E \quad (4.4.1)$$

Where  $\beta$  is the number of nearest neighbors that lie across the flux plane,  $C_N$  is the coordination number of the ion,  $n_{hkl}$  is the planar site density on the (hkl) plane (sites/area),  $N_v$  is the probability that any given site is vacant (vacancy fraction),  $1 - N_v$  is the probability that site on the left side of flux plane has an ion present,  $\nu_o$  is the vibrational frequency of the ion ( $\text{sec}^{-1}$ ), and  $\Delta \vec{P}_E$  is the probability of having sufficient energy to make a jump forward across the flux plane minus the probability of having sufficient energy to jump backward across the flux plane. The flux across the plane can be related to the ionic conductivity in the direction perpendicular to that plane using Ohm's law,  $\mathbf{J}_{[hkl]} = \sigma_{[hkl]} \mathbf{E}_{[hkl]}$ , and the relationship between current density and atomic flux,  $\mathbf{J}_{[hkl]} = q \mathbf{F}_{[hkl]}$ . Where  $\mathbf{J}_{[hkl]}$  is the current density in the [hkl] direction,  $\sigma_{hkl}$  is the ionic conductivity in the [hkl] direction,  $\mathbf{E}_{[hkl]}$  is the electric field aligned in the [hkl] direction, and  $q$  is the charge on the ion. Equation 4.4.1 rewritten in terms of the orientation dependence of the ionic conductivity is shown in Equation 4.4.2.

$$\sigma_{[hkl]}^{\vec{}} = \frac{\beta q}{C_N E} n_{hkl} N_v (1 - N_v) \nu_o \Delta \vec{P}_E \quad (4.4.2)$$

When there is no external force acting on the ions  $\Delta \vec{P}_E$  equal zero. However, when

an electric field is applied  $\Delta\mathbf{P}_E$  becomes nonzero and results in a net flux of ions in the material. The form of  $\Delta\mathbf{P}_E$  when an electric field is present is shown in Equation 4.4.3.

$$\Delta\vec{P}_E = e^{\frac{(-\Delta G)}{kT}} - e^{\frac{-(\Delta G + \epsilon)}{kT}} \quad (4.4.3)$$

Where  $\Delta G$  is the Gibbs free energy (eV) associated with making a jump to a vacant site,  $\epsilon$  (eV) is the energy due to the electric field that assists ions in making jumps with a component in the direction of the electric field,  $k$  is Boltzmann's constant (eV/K), and  $T$  is the temperature (K).  $\epsilon$  can be understood as the reduction in the energy barrier ( $\Delta G$ ) in the forward direction and increase in the energy barrier in the backward direction that results from the electric field acting on the charged ion. Since  $\epsilon/kT$  is very small ( $\sim 10^{-7}$ ), it can be taken out of the exponential using the approximation  $e^x \approx 1 + x$  for very small  $x$ . Additionally,  $\epsilon$  can be written in terms of the electric field and planar spacing as  $\epsilon = qEd_{hkl}$ . Where  $d_{hkl}$  is the spacing between (hkl) planes and  $E$  is the electric field. These changes in  $\Delta\mathbf{P}_E$  are shown in Equation 4.4.4.

$$\Delta\vec{P}_E = \frac{qEd_{hkl}}{kT} e^{\frac{-\Delta G}{kT}} \quad (4.4.4)$$

Finally Equation 4.4.4 and Equation 4.4.2 can be combined to form the relationship between orientation and conductivity in terms of material specific parameters (Equation 4.4.5).

$$\sigma_{hkl} = \frac{\beta d_{hkl} n_{hkl}}{C_N} \frac{q^2 N_v (1 - N_v) \nu_o}{kT} e^{\frac{-\Delta G}{kT}} \quad (4.4.5)$$

Equation 4.4.5 can be used to calculate the ionic conductivity in the [100] direction of single crystal GDC,  $\sigma_{100}$ . Four parameters are required for the calculation of the conductivity in the [100] direction:  $\beta$ ,  $C_N$ ,  $d_{100}$ , and  $n_{100}$ . It may be helpful for the reader to look back to Figure 1.2 in the introduction to view the simple cubic arrangement of oxygen ions in GDC's cubic fluorite structure. Figure 4.1 shows the relative position of oxygen ions on two adjacent (100) planes in GDC. Inspection of Figure 4.1 shows 1 path across the flux plane ( $\beta=1$ ) out of the total 12 paths ( $C_N=12$ ) available for every ion on the plane. The path has a jump distance of  $a_o/2$  ( $d_{100}=a_o/2$ ). It can also be observed that there are four atomic sites for every  $a_o^2$  area on the (100) plane ( $n_{100}=4/a_o^2$ ). These (100) specific components can now be put into Equation 4.4.5 to show the ionic conductivity in the [100] direction (Equation 4.4.6).

$$\sigma_{100} = \frac{1}{3a_o} \frac{q^2 N_v (1 - N_v) \nu_o}{kT} e^{\frac{-\Delta G}{kT}} \quad (4.4.6)$$

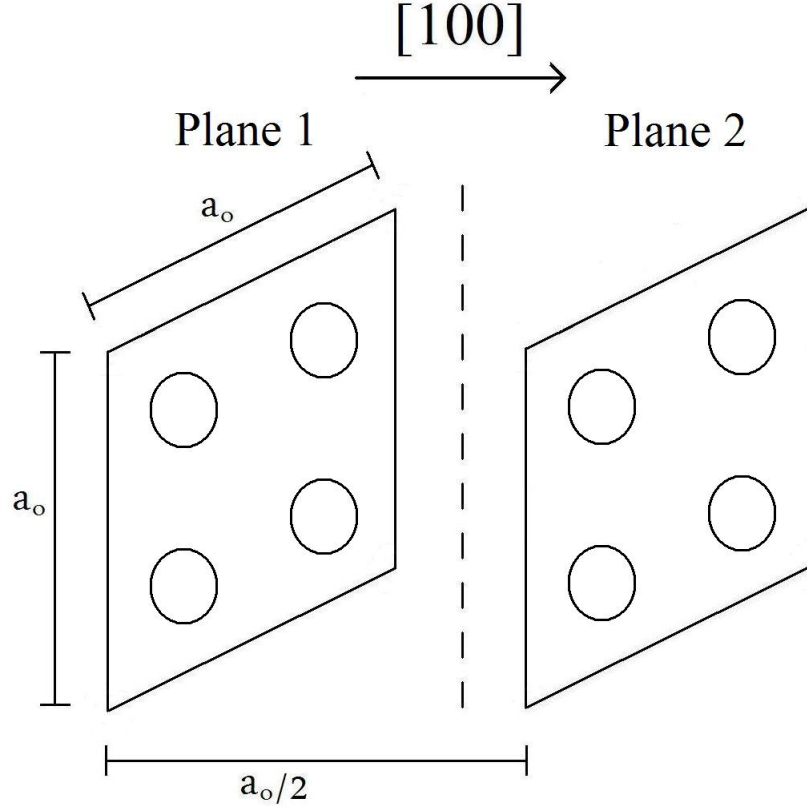


**Figure 4.1:** Schematic showing the relative positions of the atomic sites on two adjacent (100) planes. The flux plane is denoted as a dashed line.

The derivation of the relationship between the conductivity and crystallographic orientation for the [110] direction can be accomplished using the same method. Figure 4.2 shows the relative positions of atoms on two adjacent (110) planes.

Figure 4.2 shows 2 distinct paths for crossing the flux plane ( $\beta=2$ ) out of the total 12 paths ( $C_N=12$ ) available for every ion on the plane. Both paths involve jumps which are separated by  $a_o/\sqrt{2}$  ( $d_{110}=a_o/\sqrt{2}$ ). It can also be observed that there are four atomic sites for every  $\sqrt{2}a_o^2$  area on the (110) plane ( $n_{110}=4/\sqrt{2}a_o^2$ ). These (110) specific components can now be put into Equation 4.4.5 to show the ionic conductivity

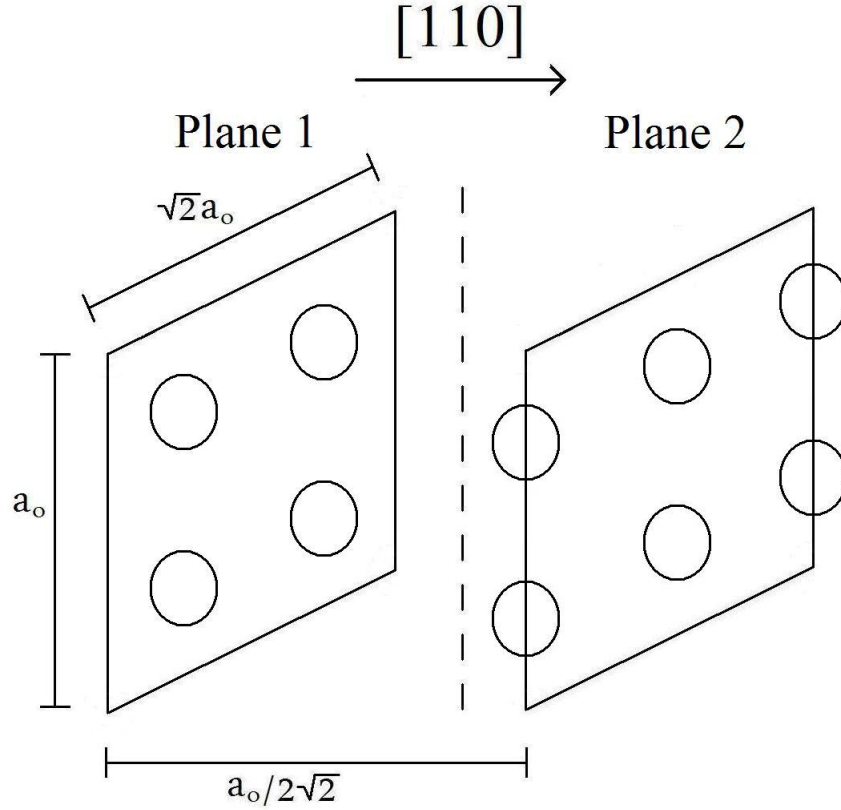


**Figure 4.2:** Schematic showing the relative positions of the atomic sites on four adjacent (110) planes. The flux plane is denoted as a dashed line.

in the  $[110]$  direction (Equation 4.4.7).

$$\sigma_{110} = \frac{1}{3a_o} \frac{q^2 N_v (1 - N_v) \nu_o}{kT} e^{\frac{-\Delta G}{kT}} \quad (4.4.7)$$

Comparison of Equations 4.4.6 and 4.4.7 shows no difference in the predicted conductivity along the two directions. One factor that could possibly change this result would be interaction energies between vacancies. If such interaction energies resulted in vacancy groupings that are more or less probable than that predicted statistically,

then the conductivities in the two direction may not be equal. With the theoretical prediction made it is now time to examine the experimental results.

X-ray diffraction and spectrally resolved optical reflectance were performed on the GDC film and showed it to be a single crystal with a thickness of  $\approx 300$  nm. Symmetric  $\theta/2\theta$  X-ray diffraction data from the film demonstrates that the GDC film is oriented with the [001] direction normal to the surface, as is the thin single crystal [001]  $\text{CeO}_2$  template.  $\phi$ -scans showed four well-defined peaks from the asymmetric (204) planes indicating that the film has a single orientation in the plane of the film and is single crystal. The azimuthal angle of the  $\phi$ -scan at which the peaks of the (204) planes occurred were used to orient the electrodes so that measurements were taken along the [100] and [110] directions in the GDC thin film.

Comparison has been made between the conductivity data of the two orientations for each of the three films. The conductivity data for the three samples of each orientation were averaged and the standard deviation of the averages calculated. This data is shown in 40°C intervals in Table 4.1.

**Table 4.1:** Comparison of the average conductivity data for the [100] and [110] orientations in the 540 to 700°C temperature range. The uncertainties represent 1 standard deviation in the fit of the data.

| Temp<br>(°C) | [100] Ave. Conductivity<br>( $\Omega^{-1}\text{cm}^{-1}$ ) | [110] Ave. Conductivity<br>( $\Omega^{-1}\text{cm}^{-1}$ ) | $\sigma_{100}/\sigma_{110}$ |
|--------------|--|--|-----------------------------|
| 700          | $3.53\text{E-}2 \pm 0.21\text{E-}2$                        | $3.32\text{E-}2 \pm 0.08\text{E-}2$                        | 1.06                        |
| 660          | $2.42\text{E-}2 \pm 0.14\text{E-}2$                        | $2.29\text{E-}2 \pm 0.07\text{E-}2$                        | 1.05                        |
| 620          | $1.60\text{E-}2 \pm 0.09\text{E-}2$                        | $1.51\text{E-}2 \pm 0.05\text{E-}2$                        | 1.06                        |
| 580          | $1.02\text{E-}2 \pm 0.06\text{E-}2$                        | $9.49\text{E-}3 \pm 0.35\text{E-}3$                        | 1.07                        |
| 540          | $6.09\text{E-}3 \pm 0.40\text{E-}3$                        | $5.67\text{E-}3 \pm 0.22\text{E-}3$                        | 1.07                        |

Inspection of Table 4.1 shows an  $\approx 6\%$  increase in the conductivity of the [100] direction compared to the [110] direction. However, the  $\approx 6\%$  difference is on the same order as one standard deviation in the [100] conductivity data indicating that there is not a statistically significant difference between the two data sets. This result does not rule out the possibility of differing conductivities in the [100] and [110] directions, but it does imply that any difference must be relatively small. One would be confident in the distinction between the two data sets if there was no overlap in two standard deviations of each data set (95.4% of the data for each set should fall within this range). Given the current uncertainty in the data, a  $\approx 20\%$  difference in the conductivities would be required to meet this criteria and show that the two data sets are independent of each other. This study concludes that the conductivities in the [100] and [110] directions does not differ by more than 20%.

## 4.5 Conclusions

In summary, conductivity measurements have been performed on single crystal GDC films along the [110] and [100] crystallographic orientations in the 500 to 700°C temperature range. The average conductivity of two data sets, containing three samples of each orientation, were compared and no statistically significant difference was observed. The theoretical model presented in this work also predicts no difference in the conductivities of the two directions. This study concludes that it is unlikely that

there is any difference between the conductivities in the  $[100]$  and  $[110]$  directions of single crystal GDC, and if a difference does exist it must be less than  $\approx 20\%$ .



## Chapter 5

Discussion: Cause of the reduced conductivity observed in samples with grain boundaries and the reduced conductivity surface/interface layer

Author: Matthew Swanson

## 5.1 Introduction

This chapter presents the most likely causes for the reduced conductivity observed in polycrystalline GDC samples compared to single crystal sample and the reduced conductivity observed in the surface/interface layer of the single crystal films.

## 5.2 Explanation of the reduced conductivity observed in the polycrystalline GDC compared to the single crystal GDC

The conductivity data for the single crystal and polycrystalline films showed that the presence of 80 nm grain boundaries significantly reduces the film's total conductivity. This result can be understood by comparing it to the greater body of work in the literature. It is well known that the ionic conductivity of GDC increases with decreasing grain size for very small grains ( $<100$  nm) and decreases with decreasing grain size for larger grains ( $>200$  nm) [3, 10–13, 16, 40]. This ionic conductivity versus grain size relationship can be explained by considering the relative volume fraction of along grain boundary, across grain boundary and bulk grain regions in samples with differing grain sizes. Each region has its own migration enthalpy and carrier concentration

and, hence, a region specific conductivity. The migration enthalpy for ions traveling along grain boundaries is likely to be significantly less than the migration enthalpy for ions traveling in the grain bulk. This is due to the reduced number of bonds on the ion traveling along the grain boundary and has been observed for a number of other solid state ion conductor systems. However, the migration enthalpy for ions traveling across a grain boundary is significantly larger than that of the bulk of the grain. This has been observed by many groups and explained in terms of a space charge layer that the ion must travel across [2, 31, 41].

For grain sizes greater than 200 nm the across grain boundary region makes up less than 1% of the total cross-sectional area of the sample and does not contribute significantly to the total ionic conduction. For these grain sizes ( $>200$  nm), increased conductivity can be realized by increasing the grain size because larger grains reduce the number of across grain boundary jumps that an ion must make. However, for very small grain sizes ( $<100$  nm) the along grain boundary region becomes a significant fraction of the total cross-sectional area. This increase in fraction of along grain boundary area with a lower migration enthalpy is probably the cause of the observed trend of increasing conductivity with decreasing grain size for the small grains. For the 80 nm grain size studied in this work it appears that the reduction in the ionic conductivity due to crossing grain boundaries still outweighs the enhancement due to the reduced migration enthalpy along grain boundaries. This results in an overall lower conductivity in the 80 nm grain size sample than the single crystal sample.

However, literature data shows the conductivity of 10 nm grain size GDC samples to be about the same as the conductivity measured for single crystal samples in this study. This suggests that around 10 nm the conductivity enhancement gained from ions traveling along grain boundaries compensates for the conductivity reduction due to ions crossing grain boundaries. These results also suggest that samples with grain sizes less than ten nanometers will likely have a higher total conductivity than single crystal GDC. However, no sample has been produced so far with a higher conductivity than the single crystal GDC and it may be very difficult to maintain grain sizes smaller than ten nanometers while the device is operated at elevated temperatures. Therefore, the conclusion of this study is that single crystal GDC will provide the highest conductivity currently available for a given device. Polycrystalline GDC with the smallest possible grain size should be used as a substitute for single crystal GDC when it is not possible to engineer the use of single crystal GDC.

### **5.3 Explanation of the reduced conductivity in the interface layer of GDC films**

The conductivity data for the five GDC films with varying thicknesses suggests the presence of a reduced conductivity interface layer present in each film. The film interface and bulk regions were compared and showed that the activation energy

for ionic transport is approximately the same in both regions, but the mobile carrier concentration appears to be significantly less in the interface layer. A reduction in the mobile carrier concentration could be caused by a reduction in the Gd concentration in this region. Reduced Gd concentration would decrease the lattice parameter of the structure and, therefore, should be observable as a peak shift in the XRD  $\theta/2\theta$  data. The  $\theta/2\theta$  data will now be analyzed to determine if such a shift is present.

Figures 5.1 and 5.2 show the  $\theta/2\theta$  plots for the (002) and (004) reflections. The peak positions of the three thickest films agree within the experimental uncertainty. Using the median peak position of the three films results in a calculated lattice parameter of 5.435Å. The lattice parameter should scale linearly with the doping content according to Vergard's Rule. A number of research groups [42–45] have empirically determined this relationship for GDC and their results are in fairly close agreement. One of the equations relating the lattice parameter to the mole fraction of  $\text{Gd}_2\text{O}_3$  is given below (Equation 5.3.1).

$$a = 5.40606 + 0.00206X \quad (5.3.1)$$

Where  $a$  is the lattice parameter (Å) and  $X$  is the mol% of  $\text{Gd}_2\text{O}_3$ . This formula predicts that the three thicker films have a composition of 15% $\text{Gd}_2\text{O}_3$  85% $\text{CeO}_2$ . This is a 5 mol% higher Gd composition than the target composition (10% $\text{Gd}_2\text{O}_3$

90%CeO<sub>2</sub>). However, although the composition of the films used in this study have never been quantitatively determined, EDS data collected from the films suggests a higher composition in the films than the sputtering target. Other researchers [22] that also deposited GDC films by RF sputtering found their films to have about 50% more Gd content than that of their sputtering target. Therefore, based on the XRD data and the results from the literature, it is likely that the true "bulk" composition of our thick films is close to 15 mol% Gd<sub>2</sub>O<sub>3</sub>.

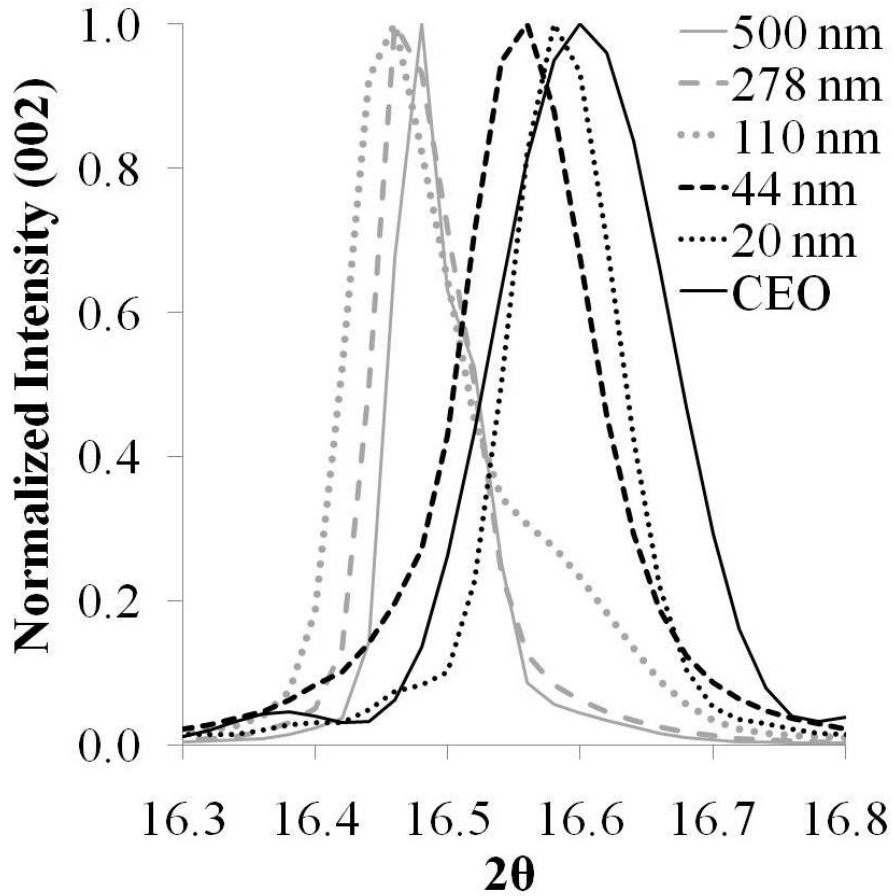


**Figure 5.1:** Plot of the  $\theta/2\theta$  data for the (002) reflection of the five GDC films and the CEO buffer layer.

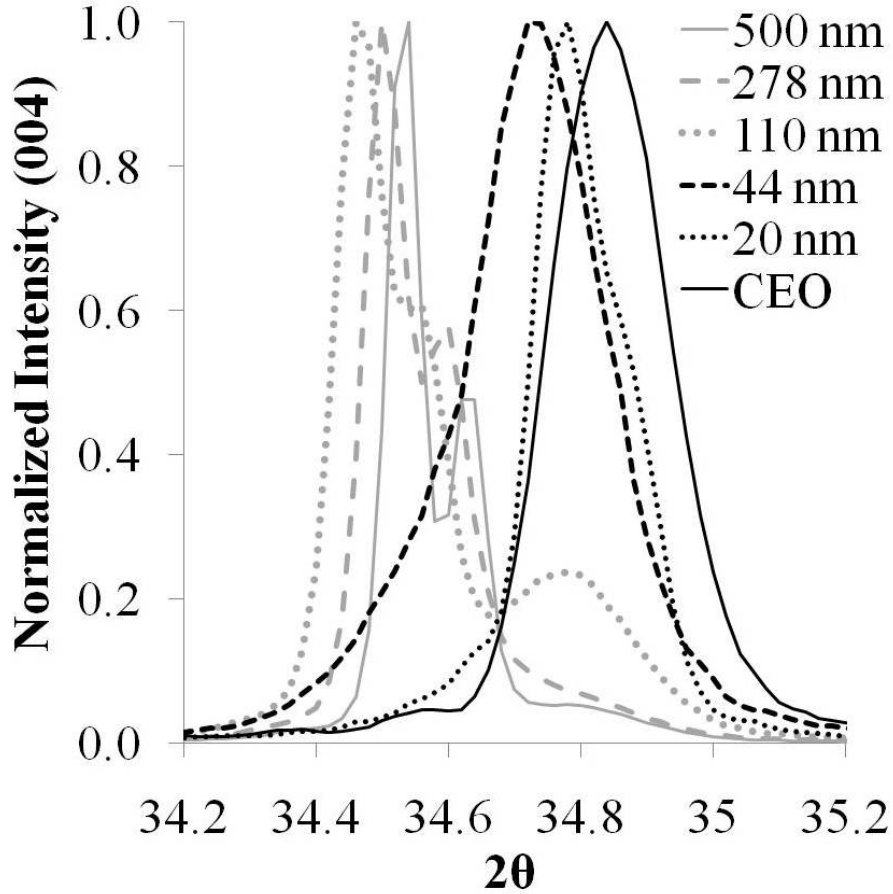


**Figure 5.2:** Plot of the  $\theta/2\theta$  data for the (004) reflection of the five GDC films and the CEO buffer layer.

The two thinnest GDC films have peak positions which are much closer to that of the undoped Ceria peak. The exact peak positions for these two films are difficult to determine because the peaks are convolved with the CEO peaks for the underlying Ceria buffer layer. However, it is clear that these peak positions are much closer to the undoped Ceria peak than they are to the three thicker films. This indicates that there is a significant reduction in the amount of Gd present in the two thinnest films. A reduction in the Gd content for the first  $\approx 50$  nanometers of the films could be a result of beginning the film growth before equilibrium conditions have been reached

and would explain the observed reduced conductivity interface layer observed in all of the GDC films.

## 5.4 Conclusions

In summary, the reduction in conductivity observed for the polycrystalline GDC samples when compared to the single crystal sample is caused by highly resistive across grain boundary regions. The reduction in the conductivity observed for the interface layer is likely due to a reduction in the Gd doping content present in the first 50 nm of every GDC single crystal film.



# Chapter 6

## Summary

In this work the effects of grain boundaries, interfaces and crystallographic orientation on the ionic conductivity of Gadolinium doped ceria were investigated. Methods to dice and prepare samples for high temperature, in-plane conductivity measurements were developed. A high temperature conductivity measurement stand was build and automated for making conductivity measurements over the 400-700°C temperature range.

The effect of grain boundaries on the ionic conductivity of GDC was investigated by the growing two GDC films that differed by the presence or absence of 80 nm grain boundaries. The single crystal conductivity data taken in the 400-700°C indicates that the ionic conductivity of the single crystal GDC film is as conductive or more

conductive than the "high-conductivity" polycrystalline GDC films studied in the literature whose large ionic conductivity was attributed to the presence of sub-micron grains. The mobility of the charge carriers was significantly reduced in the polycrystalline sample over all temperatures, leading to a reduction in the conductivity over the entire temperature range. Direct comparison of the conductivity vs. temperature data for single crystal and polycrystalline GDC thin films showed that the presence of boundaries separating 80 nm diameter grains does not enhance, but rather reduces the in-plane ionic conductivity of the GDC film.

The effect a film surface or interface on the ionic conductivity of GDC was investigated by comparing the conductivities of five single crystal films measured in the 500 to 700°C temperature range that differed only in their thickness. A clear trend of decreasing conductivity with decreasing film thickness was observed for the films larger than 100 nm. The two thinnest films had substantially reduced conductivity when compared to the thicker films. The measurements revealed that the combined impact of the film surface and film/substrate interface is to reduce the conductivity of the films. Analysis of the conductivity data suggests the presence of a layer of reduced conductivity spanning as much as 50 nm in all of the measured films. Further research is required to determine the cause and location of this less conductive layer.

The effect of the crystallographic orientation on the ionic conductivity of GDC was investigated by measuring the conductivity of single crystal GDC samples along the

[110] and [100] crystallographic orientations in the 500 to 700°C temperature range. The average conductivity of two data sets, containing three samples of each orientation, were compared and no statistically significant difference was observed. The theoretical model presented in this work also predicts no difference in the conductivities of the two directions when ions from two planes adjacent to the flux plane are considered for the [110] direction. This study concludes that it is unlikely that there is any difference between the conductivity in the [100] and [110] directions of single crystal GDC, and if a difference does exist it must be less than  $\approx 20\%$ .

In summary, this study has found that the ionic conductivity of GDC is higher in single crystals than in polycrystalline samples. There is no theoretically expected or experimentally observed difference between ionic transport in the [100] direction and the [110] direction in GDC single crystals. Furthermore, for thin film GDC, the total conductivity will be greatest for thick films ( $>500$  nm) where the interface component of the conductivity becomes less significant.

# References

- [1] Chen, L.; Chen, C. L.; Chen, X.; Donner, W.; and Y. Lin, S. W. L.; Huang, D.; Jacobson, A. *Applied Physics Letters* **2003**, *83*, 4737–4739.
- [2] Huang, H.; Gür, T. M.; Saito, Y.; Prinz, F. *Applied physics letters* **2006**, *89*, 3.
- [3] Suzuki, T.; Kosacki, I.; Anderson, H. U. *Solid State Ionics* **2002**, *151*, 11.
- [4] Rupp, J. L.; Gauckler, L. J. *Solid State Ionics* **2006**, *177*, 2513–2518.
- [5] Goodenough, J. *Annual Review of Materials Research* **2003**, *33*, 91–128.
- [6] H. Inaba, a. H. T. *Solid State Ionics* **1996**, *83*, 1–16.
- [7] Mogensen, M.; Sammes, N.; Tompsett, G. *Solid State Ionics* **2000**, *129*, 63–94.
- [8] Steele, B. *Solid State Ionics* **2000**, *129*, 16.
- [9] Swanson, M.; Tangtrakarn, N.; Sunder, M.; Moran, P. *Solid State Ionics* **2010**, *181*, 379–385.
- [10] Hui, S. R.; Roller, J.; Yick, S.; Zhang, X.; Dec’es-Petit, C.; Xie, Y.; Maric, R.; Ghosh, D. *Journal of Power Sources* **2007**, *172*, 10.
- [11] Bellino, M. G.; Lamas, D. G.; de Reca, N. E. W. *Journal of Materials Chemistry* **2008**, *18*, 4537–4542.
- [12] Bellino, M. G.; Lamas, D. G.; de Reca, N. E. W. *Advanced Materials* **2006**, *18*, 3005–3009.
- [13] Bellino, M. G.; Lamas, D. G.; de Reca, N. E. W. *Advanced Functional Materials* **2006**, *16*, 7.
- [14] Omata, T.; Goto, Y.; Otsuka-Yao-Matsuo, S. *Science and Technology of Advanced Materials* **2007**, *8*, 524–530.
- [15] Rupp, J. L.; Infortuna, A.; Gauckler, L. J. *Journal of the American Ceramics Society* **2007**, *90*, 1792–1797.

- [16] Maric, R.; Seward, S.; Faguy, P. W.; Oljaca, M. *Electrochemical and Solid-State Letters* **2003**, *6*, A91–A95.
- [17] Bera, D.; et al.. *Thin Solid Films* **2008**, *516*, 5.
- [18] Sunder, M.; Moran, P. *Journal of Electronic Materials* **2009**, *38*, 7.
- [19] der Pauw, L. V. *Philips Research Reports* **1958**, *13*, 9.
- [20] Koon, D. W. *Review of Scientific Instruments* **1989**, *60*, 7.
- [21] Chen, L.; Chen, C.; Huang, D.; Lin, Y.; Chen, X.; Jacobson, A. *Solid State Ionics* **2004**, *175*, 4.
- [22] Bieberle-Hutter, A.; Hertz, J. L.; Tuller, H. L. *Acta Materialia* **2008**, *56*, 11.
- [23] Joo, J. H.; Choi, G. *Journal of the European Ceramic Society* **2007**, *27*, 6.
- [24] Badwal.; Drennan. *Journal of Materials Science* **1987**, *22*, 9.
- [25] Chen, X.; Khor, K.; Chan, S.; Yu, L. *Materials Science and Engineering A* **2002**, *335*, 4.
- [26] Ioffe, A.; Inozemtsev, M.; Lipilin, A.; Perfilov, M.; Karpachov, S. *Physica Status Solidi A* **1975**, *30*, 6.
- [27] Dijk, T. V.; Burggaaf, A. *Physica Status Solidi A* **1981**, *63*, 6.
- [28] Lee, W.; Lee, M.; Kim, Y.; Prinz, F. *Nanotechnology* **2009**, *20*, 9.
- [29] Tuller, H. *Solid State Ionics* **2000**, *131*, 131.
- [30] Gerhardt, R.; Nowick, A.; Mochel, M.; Dumlér, I. *Journal of the American Ceramic Society* **1986**, *69*, 641–646.
- [31] Avila-Paredes, H.; Choi, K.; Chen, C.; Kim, S. *Journal of material chemistry* **2009**, *19*, 4837–4842.
- [32] Wang, D. Y.; Nowick, A. S. *Journal of Solid State Chemistry* **1980**, *35*, 325–333.
- [33] Muthukkumaran, K.; Kuppusami, P.; Mohandas, E.; Raghunathan, V.; Selladurai, S. In *International Symposium of Research Students on Materials Science and Engineering*, December 20-22, 2004, Chennai, India.
- [34] Ruiz-Trejo, E.; Sirman, J.; Baikov, Y.; Kilner, J. *Solid State Ionics* **1998**, *113*, 565–569.
- [35] Brauer, G.; Gradinger, H. Z. *Anorg. Allg. Chem.* **1954**, *276*, 209–226.

- [36] Bishop, S.; Duncan, K.; Wachsman, E. *Acta Materialia* **2009**, *57*, 10.
- [37] Karthikeyan, A.; Ramanathan, S. *Applied physics letters* **2008**, *92*, 3.
- [38] Jadhav, L.; Chourashiya, M.; Subhedar, K.; Tyagi, A.; Patil, J. *Journal of Alloys and Componds* **2009**, *470*, 4.
- [39] Shewmon, P. *Diffusion in Solids*; McGraw-Hill, 1963.
- [40] Hara, A.; Hirata, Y.; Sameshima, S.; Matsunaga, N.; Horita, T. *JOURNAL OF THE CERAMIC SOCIETY OF JAPAN* **2008**, *57*, 1851–1856.
- [41] Cho, Y. H.; Cho, P.-S.; Auchterlonie, G.; Kim, D. K.; Lee, J.-H.; Kim, D.-Y.; Park, H.-M.; Drennan, J. *Acta Materialia* **2007**, *55*, 4807–4815.
- [42] Zha, S.; Xia, C.; Meng, G. *Journal of Power Sources* **2003**, *115*, 44–48.
- [43] Singh, K.; Acharya, S. A.; Bhoga, S. S. *Ionics* **2006**, *12*, 295–301.
- [44] Mahata, T.; Das, G.; Mishra, R.; Sharma, B. *Journal of Alloys and Compounds* **2005**, *391*, 129–135.
- [45] Jadhav, L.; Chourashiya, M.; Jamale, A.; Chavan, A.; Patil, S. *Journal of Alloys and Compounds* **2010**, *506*, 739–744.

## Appendix A

The author of this dissertation has reproduced Chapter 2 from a publication in Solid State Ionics [9] of which he was the primary author. The article has been included with the permission of Elsevier. The document showing their permission is included in this section.

**ELSEVIER LICENSE  
TERMS AND CONDITIONS**

Nov 12, 2010

This is a License Agreement between Matthew M Swanson ("You") and Elsevier ("Elsevier") provided by Copyright Clearance Center ("CCC"). The license consists of your order details, the terms and conditions provided by Elsevier, and the payment terms and conditions.

**All payments must be made in full to CCC. For payment instructions, please see information listed at the bottom of this form.**

|  |  |
|--|--|
| Supplier                                     | Elsevier Limited<br>The Boulevard, Langford Lane<br>Kidlington, Oxford, OX5 1GB, UK  |
| Registered Company Number                    | 1982084  |
| Customer name                                | Matthew M Swanson  |
| Customer address                             | 2006C Woodmar Dr.<br>Houghton, MI 49931  |
| License number                               | 2546040117368  |
| License date                                 | Nov 11, 2010   |
| Licensed content publisher                   | Elsevier   |
| Licensed content publication                 | Solid State Ionics   |
| Licensed content title                       | Impact of the presence of grain boundaries on the in-plane ionic conductivity of thin film Gd-doped CeO <sub>2</sub>                       |
| Licensed content author                      | Matthew Swanson, Natee Tangtrakarn, Madhana Sunder, P.D. Moran   |
| Licensed content date                        | 29 March 2010  |
| Licensed content volume number               | 181  |
| Licensed content issue number                | 8-10   |
| Number of pages                              | 7  |
| Type of Use                                  | reuse in a thesis/dissertation   |
| Portion                                      | full article   |
| Format                                       | both print and electronic  |
| Are you the author of this Elsevier article? | Yes  |
| Will you be translating?                     | No   |
| Order reference number                       |  |
| Title of your thesis/dissertation            | INVESTIGATION INTO THE IMPACT OF INTERFACES AND CRYSTALLOGRAPHIC ORIENTATION ON THE IONIC CONDUCTIVITY OF THIN FILM GADOLINIUM-DOPED CERIA |
| Expected completion date                     | Dec 2010   |



Estimated size (number of pages) 100  
Elsevier VAT number GB 494 6272 12  
[Terms and Conditions](#)

## INTRODUCTION

1. The publisher for this copyrighted material is Elsevier. By clicking "accept" in connection with completing this licensing transaction, you agree that the following terms and conditions apply to this transaction (along with the Billing and Payment terms and conditions established by Copyright Clearance Center, Inc. ("CCC"), at the time that you opened your Rightslink account and that are available at any time at <http://myaccount.copyright.com>).

## GENERAL TERMS

2. Elsevier hereby grants you permission to reproduce the aforementioned material subject to the terms and conditions indicated.

3. Acknowledgement: If any part of the material to be used (for example, figures) has appeared in our publication with credit or acknowledgement to another source, permission must also be sought from that source. If such permission is not obtained then that material may not be included in your publication/copies. Suitable acknowledgement to the source must be made, either as a footnote or in a reference list at the end of your publication, as follows:

"Reprinted from Publication title, Vol /edition number, Author(s), Title of article / title of chapter, Pages No., Copyright (Year), with permission from Elsevier [OR APPLICABLE SOCIETY COPYRIGHT OWNER]." Also Lancet special credit - "Reprinted from The Lancet, Vol. number, Author(s), Title of article, Pages No., Copyright (Year), with permission from Elsevier."

4. Reproduction of this material is confined to the purpose and/or media for which permission is hereby given.

5. Altering/Modifying Material: Not Permitted. However figures and illustrations may be altered/adapted minimally to serve your work. Any other abbreviations, additions, deletions and/or any other alterations shall be made only with prior written authorization of Elsevier Ltd. (Please contact Elsevier at [permissions@elsevier.com](mailto:permissions@elsevier.com))

6. If the permission fee for the requested use of our material is waived in this instance, please be advised that your future requests for Elsevier materials may attract a fee.

7. Reservation of Rights: Publisher reserves all rights not specifically granted in the combination of (i) the license details provided by you and accepted in the course of this licensing transaction, (ii) these terms and conditions and (iii) CCC's Billing and Payment terms and conditions.

8. License Contingent Upon Payment: While you may exercise the rights licensed immediately upon issuance of the license at the end of the licensing process for the transaction, provided that you have disclosed complete and accurate details of your proposed use, no license is finally effective unless and until full payment is received from you (either by publisher or by CCC) as provided in CCC's Billing and Payment terms and

conditions. If full payment is not received on a timely basis, then any license preliminarily granted shall be deemed automatically revoked and shall be void as if never granted. Further, in the event that you breach any of these terms and conditions or any of CCC's Billing and Payment terms and conditions, the license is automatically revoked and shall be void as if never granted. Use of materials as described in a revoked license, as well as any use of the materials beyond the scope of an unrevoked license, may constitute copyright infringement and publisher reserves the right to take any and all action to protect its copyright in the materials.

9. Warranties: Publisher makes no representations or warranties with respect to the licensed material.

10. Indemnity: You hereby indemnify and agree to hold harmless publisher and CCC, and their respective officers, directors, employees and agents, from and against any and all claims arising out of your use of the licensed material other than as specifically authorized pursuant to this license.

11. No Transfer of License: This license is personal to you and may not be sublicensed, assigned, or transferred by you to any other person without publisher's written permission.

12. No Amendment Except in Writing: This license may not be amended except in a writing signed by both parties (or, in the case of publisher, by CCC on publisher's behalf).

13. Objection to Contrary Terms: Publisher hereby objects to any terms contained in any purchase order, acknowledgment, check endorsement or other writing prepared by you, which terms are inconsistent with these terms and conditions or CCC's Billing and Payment terms and conditions. These terms and conditions, together with CCC's Billing and Payment terms and conditions (which are incorporated herein), comprise the entire agreement between you and publisher (and CCC) concerning this licensing transaction. In the event of any conflict between your obligations established by these terms and conditions and those established by CCC's Billing and Payment terms and conditions, these terms and conditions shall control.

14. Revocation: Elsevier or Copyright Clearance Center may deny the permissions described in this License at their sole discretion, for any reason or no reason, with a full refund payable to you. Notice of such denial will be made using the contact information provided by you. Failure to receive such notice will not alter or invalidate the denial. In no event will Elsevier or Copyright Clearance Center be responsible or liable for any costs, expenses or damage incurred by you as a result of a denial of your permission request, other than a refund of the amount(s) paid by you to Elsevier and/or Copyright Clearance Center for denied permissions.

#### LIMITED LICENSE

The following terms and conditions apply only to specific license types:

15. **Translation:** This permission is granted for non-exclusive world **English** rights only unless your license was granted for translation rights. If you licensed translation rights you may only translate this content into the languages you requested. A professional translator must perform all translations and reproduce the content word for word preserving the integrity of the article. If this license is to re-use 1 or 2 figures then permission is granted for non-exclusive world rights in all languages.

16. **Website:** The following terms and conditions apply to electronic reserve and author websites:

**Electronic reserve:** If licensed material is to be posted to website, the web site is to be password-protected and made available only to bona fide students registered on a relevant course if:

This license was made in connection with a course,

This permission is granted for 1 year only. You may obtain a license for future website posting,

All content posted to the web site must maintain the copyright information line on the bottom of each image,

A hyper-text must be included to the Homepage of the journal from which you are licensing at <http://www.sciencedirect.com/science/journal/xxxxx> or the Elsevier homepage for books at <http://www.elsevier.com> , and

Central Storage: This license does not include permission for a scanned version of the material to be stored in a central repository such as that provided by Heron/XanEdu.

17. **Author website** for journals with the following additional clauses:

All content posted to the web site must maintain the copyright information line on the bottom of each image, and

the permission granted is limited to the personal version of your paper. You are not allowed to download and post the published electronic version of your article (whether PDF or HTML, proof or final version), nor may you scan the printed edition to create an electronic version,

A hyper-text must be included to the Homepage of the journal from which you are licensing at <http://www.sciencedirect.com/science/journal/xxxxx> , As part of our normal production process, you will receive an e-mail notice when your article appears on Elsevier's online service ScienceDirect ([www.sciencedirect.com](http://www.sciencedirect.com)). That e-mail will include the article's Digital Object Identifier (DOI). This number provides the electronic link to the published article and should be included in the posting of your personal version. We ask that you wait until you receive this e-mail and have the DOI to do any posting.

Central Storage: This license does not include permission for a scanned version of the material to be stored in a central repository such as that provided by Heron/XanEdu.

18. **Author website** for books with the following additional clauses:

Authors are permitted to place a brief summary of their work online only.

A hyper-text must be included to the Elsevier homepage at <http://www.elsevier.com>

All content posted to the web site must maintain the copyright information line on the bottom of each image

You are not allowed to download and post the published electronic version of your chapter, nor may you scan the printed edition to create an electronic version.

Central Storage: This license does not include permission for a scanned version of the material to be stored in a central repository such as that provided by Heron/XanEdu.

19. **Website** (regular and for author): A hyper-text must be included to the Homepage of the journal from which you are licensing at <http://www.sciencedirect.com/science/journal/xxxxx>. or for books to the Elsevier homepage at <http://www.elsevier.com>

## Appendix B

This section derives the relationship between the ionic conductivity in the [100] and [110] directions for ions in a face centered cubic arrangement.

$$\sigma_{hkl} = \frac{\beta d_{hkl} n_{hkl}}{C_N} \frac{q^2 N_v (1 - N_v) \nu_o}{kT} e^{\frac{-\Delta G}{kT}} \quad (6.0.1)$$

Equation 6.0.1 can be used to calculate the ionic conductivity in the [100] direction of single crystal GDC,  $\sigma_{100}$ . Four parameters are required for the calculation of the conductivity in the [100] direction:  $\beta$ ,  $C_N$ ,  $d_{100}$ , and  $n_{100}$ . It may be helpful for the reader to look back to Figure 1.2 in the introduction to view the FCC arrangement of oxygen ions in GDC's cubic fluorite structure. Figure 6.1 shows the relative position of oxygen ions on two adjacent (100) planes in GDC. Inspection of Figure 6.1 shows 4 distinct paths for crossing the flux plane ( $\beta=4$ ) out of the total 12 paths ( $C_N=12$ ) available for every ion on the plane. All of the the paths involve jumps from plane 1 to plane 2 which are separated by  $a_o/2$  ( $d_{100}=a_o/2$ ). It can also be observed that there are two atomic sites for every  $a_o^2$  area on the (100) plane ( $n_{100}=2/a_o^2$ ). These (100) specific components can now be put into Equation 6.0.1 to show the ionic conductivity in the [100] direction (Equation 6.0.2).

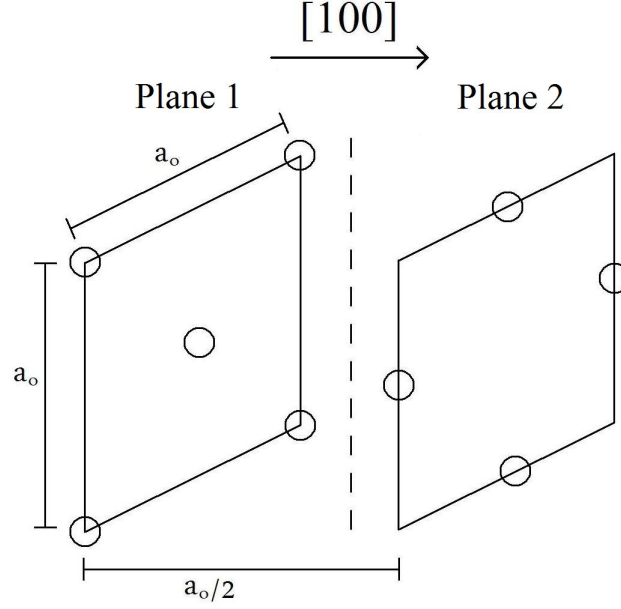


**Figure 6.1:** Schematic showing the relative positions of the atomic sites on two adjacent (100) planes. The flux plane is denoted as a dashed line.

$$\sigma_{100} = \frac{1}{3a_o} \frac{q^2 N_v (1 - N_v) \nu_o}{kT} e^{\frac{-\Delta G}{kT}} \quad (6.0.2)$$

The derivation of the relationship between the conductivity and crystallographic orientation for the [110] direction is more complicated than the [100] case. Figure 6.2 shows the relative positions of atoms on four adjacent (110) planes. It can be seen in Figure 6.2 that there are 6 distinct paths across the flux plane ( $\beta=6$ ): one path from plane 1 to plane 3 directly in the [110] direction, one path from plane 2 to plane 4 directly in the [110] direction, and 4 paths from plane 2 to plane 3 which are at an angle to the [110] direction. These two different alignments of jump directions to the [100] direction, and, hence to the applied electric field, result in different values for the  $\Delta \mathbf{P}_E$  term depending on which site across the flux plane is considered. These

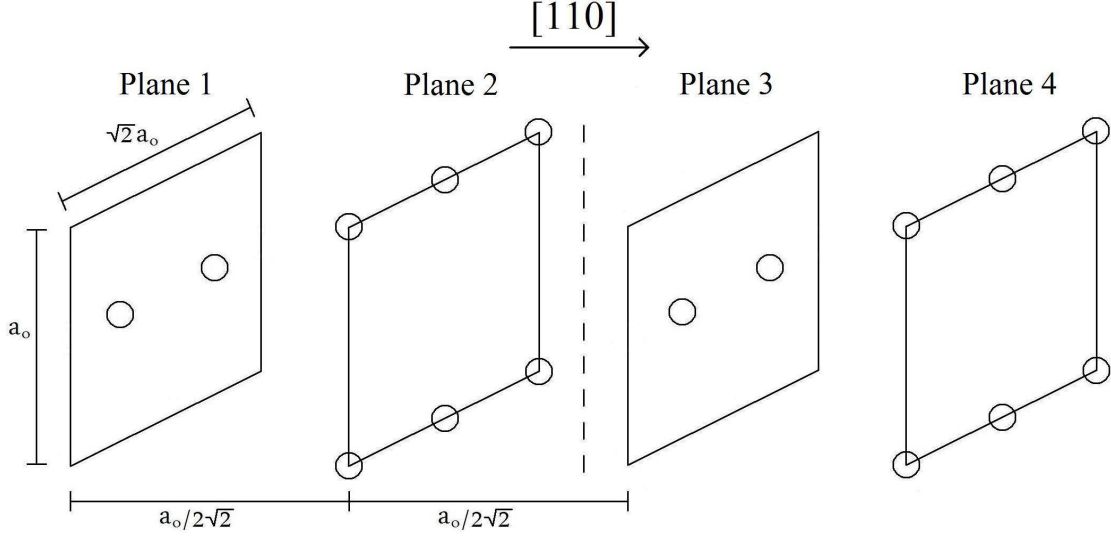


**Figure 6.2:** Schematic showing the relative positions of the atomic sites on four adjacent (110) planes. The flux plane is denoted as a dashed line.

complications to the problem result in the inability to directly apply Equation 6.0.1 to the [110] case. It will be seen that a more descriptive and generalize form of Equation 6.0.1 can be written as follows (Equation 6.0.3).

$$\sigma_{hkl} = \sum_{i=1}^{\beta} \frac{d_{hkl}^i n_{hkl}}{C_N} \frac{q^2 N_v (1 - N_v) \nu_o}{kT} e^{\frac{-\Delta G}{kT}} \quad (6.0.3)$$

Where  $d_{hkl}$  is the spacing between the two planes the ion jumps between for the  $i$ th path across the flux plane. This generalized form of directional conductivity relationship will now be derived for the case of conductivity along the [110] direction.

The conductivity in the [110] direction can be derived by considering the flux across a plane perpendicular to the [100] direction. Figure 6.2 shows two adjacent planes on

the left of the flux plane that each contain ions that have a nearest neighbor on the right side of the flux plane. One can now consider the flux across the plane from three types of flux events: (1) the ion on plane 1 jumping across the flux plane, (2) the ion on plane 2 jumping across the flux plane, and (3) both ions simultaneously jumping across the flux plane. These three events are "mutually exclusive" and so they can be summed to determine the total flux across the flux plane. This relationship is shown in Equation 6.0.4.

$$F_{Total} = F_{P1} + F_{P2} + F_{P12} \quad (6.0.4)$$

Where  $F_{Total}$  is the total ionic flux,  $F_{P1}$  is the flux due to the representative ion on plane 1 jumping across the flux plane,  $F_{P2}$  is the flux due to the representative ion on plane 2 jumping across the flux plane, and  $F_{P12}$  is the flux due to both ions simultaneously jumping across the flux plane. It can be readily observed that both  $F_{P1}$  and  $F_{P2}$  will be dependent on the probability of having sufficient energy to make a jump forward across the flux plane minus the probability of having sufficient energy to jump backward across the flux plane,  $\Delta\mathbf{P}_E$ . At the same time  $F_{P12}$  will be depended on the square of this term,  $\Delta\mathbf{P}_E^2$ , due to the requirement that both ions have sufficient energy to make the jumps. Since  $\Delta\mathbf{P}_E$  is very small ( $\sim 10^{-5}$ ) its square is extremely small ( $\sim 10^{-9}$ ) and can be considered negligible when being added to terms that are four to five orders of magnitude larger. Then only the  $F_{P1}$  and

$F_{P2}$  components of the flux need to be considered in the calculation of the total flux.

In general the flux for an ion on any given plane can be written as the product of three terms: (1) the planar density ( $n_{hkl}$ ), (2) the vibration frequency ( $\nu_o$ ), (3) the probability that the ion will contribute to flux across the flux plane. The first two terms will be constant for any geometry considered. The third term may vary depending on the crystallographic/electric field geometry and can be further broken down into the product of three probabilities for conditions that must all be satisfied in order to produce a net flux across the flux plane (the conditions are emphasized with italics): (1) probability that the *ion is vibrating in the direction of a vacancy across the flux plane* ( $P_{vib}$ ), (2) probability that the *ion has sufficient energy to jump into the vacancy* ( $\Delta P_E$ ), and (3) probability that *there is a vacancy in the site the ion is vibrating towards* ( $P_v$ ). These probabilities are dependent on the number of vacancies present and the alignment of the jump path with the electric field. The approach to determine  $F_{P1}$  and  $F_{P2}$  is to sum the flux contributions from all of the possible vacancy arrangements that could be present across the flux plane for the ions on planes 1 and 2. The functional form of this approach is shown in Equation 6.0.5.

$$F = n_{hkl}(1 - N_v)\nu_o \sum_{j=1}^{A_T} P_{vib}(j)\Delta P_E(j)P_v(j) \quad (6.0.5)$$

Where the function is summed for all possible vacancy arrangements ( $A_T$ ) and all



three probabilities are dependent on the  $j$ th arrangement of vacancies.

$F_{P1}$  has only one path across the flux plane and the probability that a vacancy is in that site is  $N_v$ . Also the single path is directly aligned with the electric field. The reduction in the energy barrier associated with the direct alignment with the electric field will be called  $\epsilon_\alpha$ . The equation for  $F_{P1}$  is given below (Equation 6.0.6).

$$F_{P1} = 2n_{110}\nu_o \frac{\epsilon_\alpha}{12kT} N_v(1 - N_v)e^{\frac{-\Delta G}{kT}} \quad (6.0.6)$$

The calculation of  $F_{P2}$  is more complicated and requires the addition of five mutually exclusive cases: (1) flux across the plane when the representative ion on plane 2 has one vacant site to jump to across the flux plane ( $F^1_{P2}$ ), (2) flux across the plane when the ion on plane 2 has two vacant sites to jump to across the flux plane ( $F^2_{P2}$ ), (3) flux across the plane when the ion on plane 2 has three vacant sites to jump to across the flux plane ( $F^3_{P2}$ ), (4) flux across the plane when the ion on plane 2 has four vacant sites to jump to across the flux plane ( $F^4_{P2}$ ), (5) flux across the plane when the ion on plane 2 has five vacant site to jump to across the flux plane ( $F^5_{P2}$ ). An expression showing this relationship is given in Equation 6.0.7.

$$F_{P2} = F^1_{P2} + F^2_{P2} + F^3_{P2} + F^4_{P2} + F^5_{P2} \quad (6.0.7)$$

Where the superscript on each term denotes the number of vacancies present on the five possible sites to which the ion on plane 2 can jump.

$F^1_{P2}$  can be determined by summing the flux contributions for the ion on plane 2 when there is a single vacancy present in each of the five possible positions across the flux plane (four arrangements with one vacancy on plane 3 and one arrangement with one vacancy on plane 4). This relationship is shown below (Equation 6.0.8).

$$F^1_{P2} = 4F^1_{P21} + F^1_{P22} \quad (6.0.8)$$

Where the second numeric subscript denotes the arrangement of the vacancy for each of the terms. One of the arrangements has a single vacancy is on plane 4 ( $F^1_{P22}$ ) and will have a reduction in the energy barrier of  $\epsilon_\alpha$ . The other four arrangements ( $4F^1_{P21}$ ) are located on plane 3 and have a reduction in the energy barrier that is half of the  $\epsilon_\alpha$  value. This energy reduction will be called  $\epsilon_\beta$ .  $P_{vib}$  will equal 1/12 for all of the arrangements since there is only one possible vacancy location to vibrate towards across the flux plane. For this single vacancy case,  $P_v$ , is equal to  $N_v(1-N_v)^4$ . This quantity is the probability having a single vacancy out of the 5 possible positions. The expression for  $F^1_{P2}$  is shown below (Equation 6.0.9).

$$F_{P2}^1 = n_{110}\nu_o(1 - N_v)[4\frac{\epsilon_\beta}{12kT} + \frac{\epsilon_\alpha}{12kT}]N_v^1(1 - N_v)^4e^{\frac{-\Delta G}{kT}} \quad (6.0.9)$$

It can be seen in Equation 6.0.9 that the flux contributions from the 4 equivalent arrangements have been collected together. This practice of combining the flux contributions from equivalent vacancy arrangements will be performed throughout the derivation to reduce redundancy. Next one can calculate the contribution to the total flux when two vacancies are present on the 5 possible jump positions.

There are 10 mutually exclusive vacancy arrangements that must be considered for  $F_{P2}^2$ . Four of the configurations ( $4F_{P21}^2$ ) have one vacancy on plane 3 and one vacancy on plane 4, and six configurations ( $6F_{P22}^2$ ) have two vacancies on plane 3. This relationship is shown in Equation 6.0.10.

$$F_{P2}^2 = 4F_{P21}^2 + 6F_{P22}^2 \quad (6.0.10)$$

The four configurations with one vacancy on plane 3 and one vacancy on plane 4 will each have a 1/12 chance at approaching an energy barrier reduced by  $\epsilon_\alpha$  and a 1/12 chance at approaching an energy barrier reduced by  $\epsilon_\beta$ . The six configurations with two vacancies on plane 3 will have a 2/12 chance at approaching an energy barrier reduced by  $\epsilon_\beta$ . All of the vacancy configurations have the same chance of having two

out of the five sites vacant ( $P_v = N_v^2(1-N_v)^3$ ). The expression for  $F_{P2}^2$  is shown in equation Equation 6.0.11.

$$F_{P2}^2 = n_{110}\nu_o(1 - N_v)[4(\frac{\epsilon_\beta}{12kT} + \frac{\epsilon_\alpha}{12kT}) + 6(\frac{2\epsilon_\beta}{12kT})]N_v^2(1 - N_v)^3e^{\frac{-\Delta G}{kT}} \quad (6.0.11)$$

There are 10 mutually exclusive vacancy arrangements that must be considered for  $F_{P2}^3$  as well. Four of the configurations ( $4F_{P21}^3$ ) have three vacancies on plane 3 and six of the configurations ( $6F_{P22}^3$ ) have two vacancies on plane 3 and one on plane 4. This relationship is shown in Equation 6.0.12.

$$F_{P2}^3 = 4F_{P21}^3 + 6F_{P22}^3 \quad (6.0.12)$$

The four configurations with three vacancies on plane 3 will each have a 3/12 chance at approaching an energy barrier reduced by  $\epsilon_\beta$ . The six configurations with two vacancies on plane 3 and one on plane 4 will have a 2/12 chance at approaching an energy barrier reduced by  $\epsilon_\beta$  and a 1/12 chance at approaching an energy barrier reduced by  $\epsilon_\alpha$ . All of the vacancy configurations have the same chance of having three out of the five sites vacant ( $P_v = N_v^3(1-N_v)^2$ ). The expression for  $F_{P2}^3$  is shown in equation Equation 6.0.13.

$$F_{P2}^3 = n_{110}\nu_o(1 - N_v)[4(\frac{3\epsilon_\beta}{12kT}) + 6(\frac{2\epsilon_\beta}{12kT} + \frac{\epsilon_\alpha}{12kT})]N_v^3(1 - N_v)^2e^{\frac{-\Delta G}{kT}} \quad (6.0.13)$$

There are 5 mutually exclusive vacancy arrangements that must be considered for  $F_{P2}^4$ . Four of the configurations ( $4F_{P21}^4$ ) have three vacancies on plane 3 and one on plane 4 and one configuration ( $1F_{P22}^4$ ) with all four vacancies on plane 3. This relationship is shown in Equation 6.0.14.

$$F_{P2}^4 = 4F_{P21}^4 + 1F_{P22}^4 \quad (6.0.14)$$

The four configurations with three vacancies on plane 3 and one on plane 4 will have a 3/12 chance at approaching an energy barrier reduced by  $\epsilon_\beta$  and a 1/12 chance at approaching an energy barrier reduced by  $\epsilon_\alpha$ . The single configuration with all four vacancies on plane 3 will have a 4/12 chance at approaching an energy barrier reduced by  $\epsilon_\beta$ . All of the vacancy configurations have the same chance of having four out of the five sites vacant ( $P_v = N_v^4(1-N_v)^1$ ). The expression for  $F_{P2}^4$  is shown in equation Equation 6.0.15.

$$F_{P2}^4 = n_{110}\nu_o(1 - N_v)[4(\frac{3\epsilon_\beta}{12kT} + \frac{\epsilon_\alpha}{12kT}) + \frac{4\epsilon_\beta}{12kT}]N_v^4(1 - N_v)^1e^{\frac{-\Delta G}{kT}} \quad (6.0.15)$$

There is only one arrangement that must be considered for  $F_{P2}^5$ . This configuration consists of all five positions occupied by vacancies ( $1F_{P21}^5$ ). This relationship is shown in Equation 6.0.16.

$$F_{P2}^5 = 1F_{P21}^5 \quad (6.0.16)$$

The single configuration with four vacancies on plane 3 and one on plane 4 will have a 4/12 chance at approaching an energy barrier reduced by  $\epsilon_\beta$  and a 1/12 chance at approaching an energy barrier reduced by  $\epsilon_\alpha$ . The probability that all five positions are vacant is given by  $P_v = N_v^5$ . The expression for  $F_{P2}^5$  is shown in equation Equation 6.0.17.

$$F_{P2}^5 = n_{110}\nu_o(1 - N_v)\left[\frac{4\epsilon_\beta}{12kT} + \frac{\epsilon_\alpha}{12kT}\right]N_v^5 e^{\frac{-\Delta G}{kT}} \quad (6.0.17)$$

These flux components can now be summed according to Equations 6.0.4 and 6.0.7.

The result is shown in Equation 6.0.18

$$\begin{aligned}
F_{Total} = & \frac{n_{110}\nu_o(1 - N_v)}{12kT} e^{\frac{-\Delta G}{kT}} * \\
& \epsilon_\alpha N_v + (4\epsilon_\beta + \epsilon_\alpha) N_v^1 (1 - N_v)^4 + \\
& (4\epsilon_\beta + 12\epsilon_\beta + 4\epsilon_\alpha) N_v^2 (1 - N_v)^3 + \\
& (12\epsilon_\beta + 12\epsilon_\beta + 6\epsilon_\alpha) N_v^3 (1 - N_v)^2 + \\
& (4\epsilon_\beta + 4\epsilon_\alpha + 12\epsilon_\beta) N_v^4 (1 - N_v)^1 + (4\epsilon_\beta + \epsilon_\alpha) N_v^5]
\end{aligned} \tag{6.0.18}$$

Equation 6.0.18 can be rewritten to group the  $\epsilon_\alpha$  and  $\epsilon_\beta$  terms. This is shown in Equation 6.0.19.

$$\begin{aligned}
F_{Total} = & \frac{n_{110}\nu_o(1 - N_v)}{12kT} e^{\frac{-\Delta G}{kT}} * \\
& \epsilon_\alpha N_v + (\epsilon_\alpha N_v^1 (1 - N_v)^4 + 4\epsilon_\alpha N_v^2 (1 - N_v)^3 + 6\epsilon_\alpha N_v^3 (1 - N_v)^2 + \\
& 4\epsilon_\alpha N_v^4 (1 - N_v)^1 + \epsilon_\alpha N_v^5 + (4\epsilon_\beta N_v^1 (1 - N_v)^4 + 16\epsilon_\beta N_v^2 (1 - N_v)^3 + \\
& 24\epsilon_\beta N_v^3 (1 - N_v)^2 + 16\epsilon_\beta N_v^4 (1 - N_v)^1 + 4\epsilon_\beta N_v^5]
\end{aligned} \tag{6.0.19}$$

The following mathematical relationship can be used to remove the various powers of  $N_v$  (Equation 6.0.20).

$$X = X^1(1 - X)^4 + 4X^2(1 - X)^3 + 6X^3(1 - X)^2 + 4X^4(1 - X)^1 + X^5 \tag{6.0.20}$$

Equation 6.0.19 can now be greatly simplified by the use of Equation 6.0.20. The result is shown in Equation 6.0.21.

$$F_{Total} = \frac{n_{110}\nu_o(1 - N_v)}{12kT} N_v e^{\frac{-\Delta G}{kT}} [2\epsilon_\alpha + 4\epsilon_\beta] \quad (6.0.21)$$

Substituting the expressions for  $\epsilon_\alpha$  and  $\epsilon_\beta$  in terms of the spacing of the planes that the ion jumps between ( $d_{hkl}$ ) and using the generic forms of  $n_{hkl}$  and  $C_N$  results in Equation 6.0.22.

$$\sigma_{hkl} = \sum_{i=1}^{\beta} \frac{d_{hkl}^i n_{hkl}}{C_N} \frac{q^2 N_v (1 - N_v) \nu_o}{kT} e^{\frac{-\Delta G}{kT}} \quad (6.0.22)$$

Where  $d_{hkl}$  is the spacing between the two planes the ion jumps between, for the  $i$ th path across the flux plane. Inspection of Equation 6.0.3 reveals that this mathematical construct is the same as summing the conductivity contributions from each one of the possible nearest neighbor jumps across the flux plane. This result shows that it is not necessary to consider all possible combination of vacancies across the flux plane, because all combinations are already accounted for when treating the jumps to nearest neighbor sites as independent contributions to the conductivity.

Substituting the values of  $n_{110}$ ,  $\epsilon_\alpha$ , and  $\epsilon_\beta$  into Equation 6.0.21 and converting the



flux to conductivity, as shown earlier, results in Equation 6.0.23

$$\sigma_{110} = \frac{1}{3a_o} \frac{q^2 N_v (1 - N_v) \nu_o}{kT} e^{\frac{-\Delta G}{kT}} \quad (6.0.23)$$

Comparison of Equations 6.0.2 and 6.0.23 shows no difference in the predicted conductivity along the two directions.